Monthly Notices
of the
ROYAL ASTRONOMICAL SOCIETY

MNRAS **493,** 5944–5971 (2020)
Advance Access publication 2020 March 9

doi:10.1093/mnras/staa557

Axion structure formation – II. The wrath of collapse

Erik W. Lentz,[1,2]★ Thomas R. Quinn[3] and Leslie J. Rosenberg[2]

[1]*Institut für Astrophysik, Georg-August Universität Göttingen, Göttingen, D-Deutschland 37707, Germany*
[2]*Department of Physics, University of Washington, Seattle, WA 98195-1560, USA*
[3]*Department of Astronomy, University of Washington, Seattle, WA 98195-1580, USA*

Accepted 2020 February 10. Received 2020 January 29; in original form 2019 August 22

ABSTRACT

The first paper in this series showed that quantum chromodynamic axion dark matter, as a highly correlated Bose fluid, contains extra-classical physics on cosmological scales. The source of the derived extra-classical physics is exchange–correlation interactions induced by the constraints of symmetric particle exchange and interaxion correlations from self-gravitation. The paper also showed that the impact of extra-classical physics on early structure formation is marginal, as the exchange–correlation interaction is inherently non-linear. This paper continues the study of axion structure formation into the non-linear regime, considering the case of full collapse and virialization. The *N*-body method is chosen to study the collapse, and its algorithms are derived for a condensed Bose fluid. Simulations of isolated gravitational collapse are performed for both Bose and cold dark matter fluids using a prototype *N*-body code. Unique Bose structures are found to survive even the most violent collapses. Bose post-collapse features include dynamical changes to global structures, creation of new broad sub-structures, violations of classical binding energy conditions, and new fine structures. Effective models of the novel structures are constructed and possibilities for their observation are discussed.

Key words: methods: numerical – galaxies: formation – galaxies: haloes – galaxies: structure – dark matter.

1 INTRODUCTION

The first paper of this series (Lentz, Quinn & Rosenberg 2019; ASF1) presents a new model of structure formation for relic quantum chromodynamic (QCD) axions, which more fully details the correlated nature of condensed self-gravitating Bose fluids in a Friedmann–Lemaître–Robertson–Walker (FLRW) cosmology (Misner, Thorne & Wheeler 1973). Such a model did not exist in the literature previously as there is contention over the appropriate scope of condensation for a gravitationally interacting medium. The various perspectives in this debate lead to drastically different conclusions as to the existence of axion structures distinct from collision-less cold dark matter (CDM), with many supporting the position that unique structures do not exist beyond the de Broglie scale (for instance, see Berges & Jaeckel 2015; Davidson 2015; Guth, Hertzberg & Prescod-Weinstein 2015), while others promote the existence of super-de Broglie effects (Sikivie & Yang 2009; Erken et al. 2012; Banik & Sikivie 2016). This axion structure formation series of papers aims to resolve the extent to which degeneracy, correlation, and quantum mechanics beyond the mean field can create structure in self-gravitating bosonic dark matter (DM) that is distinct from CDM.

ASF1 and Lentz, Quinn & Rosenberg (2020) (LQR) begin the process by developing a realistic model of weak-gravity non-relativistic condensate dynamics, mapping the covariant quantum theory of the axion field on to many-body quantum mechanics after the radiation-dominated era. By constructing a Hamiltonian of the co-moving non-relativistic many-body axion system, explicit solutions of the many-body state are found in ASF1 in the Compton–Newtonian limit. A more precise definition of condensation can also be formed in this context, which differs subtly but significantly from standard mean field theory (MFT). The resulting motion of such a maximally condensed fluid is found to be different from a pressure-less fluid, MFT, or classical field, even on super-de Broglie length-scales, owing to its conformal two-body correlation function. Also, it is worth noting that self-gravitating axion MFTs and classical fields in the literature produce pressure-less fluids in the super-de Broglie limit (Berges & Jaeckel 2015; Davidson 2015; Guth et al. 2015; Mocz et al. 2018; Veltmaat, Niemeyer & Schwabe 2018). Sample behaviour of the correlation function from ASF1, for simple Bose condensates and Fermi fluids near the condensed limit, can be viewed in Fig. 1. As there are no intrinsic scales for this purely self-gravitating system, the departure from unity of the dimensionless correlation function is measured by global deviations from single-particle separability.

The model laid out in ASF1 contains new physics and the potential for new DM structures inherited from a highly correlated

★ E-mail: erik.lentz@uni-goettingen.de

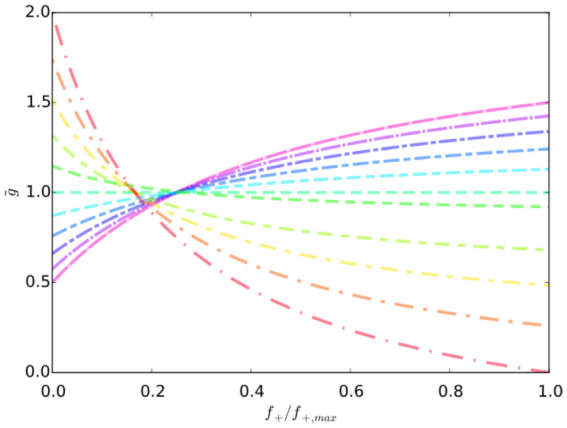

Figure 1. Correlation functions over fractional density for several near-degenerate systems, both bosonic and fermionic. The lines that lie below unity at the maximum of the distribution function (DF) $f_+/f_{+,\,\mathrm{max}} = 1$ (red to green; dash–dotted to dashed) are from non-interacting Fermi distributions. The lines at and above unity (green to violet; dashed to near-solid) are from condensed scalar Bose distributions. f_+ is formally defined in equation (2). From fig. C1 of Lentz et al. (2019). A colour version is available online.

axion condensate, on conceivably any scale so long as the Newtonian and super-de Broglie conditions hold. The self-gravitating exchange–correlation interactions are inherently non-linear, making them invisible in linear analyses of an early universe close to the homogeneous and separable limits. This null result is demonstrated in ASF1 using linear perturbation theory on an otherwise standard depiction of structure near the era of recombination. Additional allowances are required to be given to the extra-classical forces in order to separate the correlation effects formally from zero.

This paper addresses whether or not the unique physics in Bose condensate dynamics can impact the more violent phases of structure formation. Namely, we ask whether unique Bose structures form during non-linear gravitational collapse, through shell crossing, and survive into virialization. It is difficult to apply analytic techniques to such computations, but an appropriate numerical method can accurately and stably perform these calculations. The *N*-body method, and more generally the method of characteristics (MOC), will be the numerical technique for this paper due to its success in solving for classical infall (Courant & Hilbert 1953; Dehnen & Read 2011). *N*-body methods have proven useful in calculating all phases of DM structure formation (Diemand, Moore & Stadel 2005; Angulo et al. 2012; Pillepich et al. 2018). *N*-body methods are particularly well-suited for modelling CDM, as they can capture the non-equilibrium dynamics and reliably model force fields of collision-less fluids in phase space over many orders of magnitude. Further, many sophisticated and highly scalable platforms already exist to simulate such systems. It is expected to be straight forward to incorporate Bose infall dynamics into such a platform.

It is prudent to first test the Bose model in a simple implementation prior to the full development, testing, and detailed simulation using a large and complex platform. This second paper of the axion structure formation series derives an *N*-body method for Bose infall and tests it in a simple implementation on a range of collapses using a prototype code. The results of these simulations give a preliminary indication of whether or not structures unique to Bose fluids can survive gravitational collapse. The remainder of this paper is structured as follows: Section 2 reviews the continuum model of Bose structure formation; Section 3 demonstrates the Bose model on rotating spherical shells, building intuition for the role played by exchange-correlation on infall; Section 4 converts the continuum description into an *N*-body algorithm, and introduces the small-scale *N*-body code and its gravity solver; Section 6 introduces the series of preliminary simulations performed for both classical and Bose gravitational collapse and their initial conditions; Section 7 presents the results from the simulations, showing that unique structures not only exist in, but also in some cases thrive on, violent collapse; Section 8 discusses the simulations and begins to build some intuition for the novel resolved Bose structures found, exploring several observables for search; and Section 9 presents prospects for further investigation, including the incorporation of these algorithms into one of the large-scale *N*-body codes.

2 CONDENSATE STRUCTURE FORMATION

The many-body quantum state of N relic axions after the matter-radiation transition is governed by a co-moving Schrödinger equation of dimension $3N + 1$. ASF1 and LQR found solutions of this equation to be more compactly described by interaxion correlators than the standard single product Fock space representation used by many MFTs. Even with this insight, a general galactic halo contains far too many axions to simulate without a reduction in the degrees of freedom. ASF1 and LQR also found it possible via the Runge–Gross theorem (Runge & Gross 1984) to reduce the dynamics of the full system to tracking the motions of a single-body mass density. This reduction is performed in ASF1 and LQR using a Wigner transformation (Wigner 1932), converting the wave-function representation to a pseudo-distribution function (pseudo-DF) over the many-body phase space, then integrating over $N - 1$ single-particle phase spaces. The impact of position-momentum complementarity is trivialized by the super-de Broglie limit in which the halo is evaluated, effectively converting the Wigner function to a true DF. Fortunately, modern cosmological simulations are smoothed over spatial scales of the order of many parsecs, far longer than the expected QCD axion wavelengths, removing the influence of de Broglie-level dynamics. The only component of the correlated self-gravitating many-body state to survive super-de Broglie smoothing and integration over all but a single phase space is the conformal two-body correlation function

$$\tilde{g} = \frac{C + \lambda_1 f_+}{1 + \lambda_2 f_+}, \tag{1}$$

where C is, for this study, a measure of the axion's correlation at zero density and an a priori unknown initial condition, λ_1 and λ_2 are Lagrange multipliers introduced in ASF1 and LQR, and f_+ is a two-body function composed of the symmetric combination of single-body DFs

$$f_+ = \frac{1}{2}\left(f^{(1)}(w_1, t) + f^{(1)}(w_2, t)\right), \tag{2}$$

where $w = (\boldsymbol{x}, \boldsymbol{v})$, and $f^{(1)}$ is the single-body DF. Such a long-range correlation function is expected as the interaxion correlator wavelength far exceeds the single particle de Broglie wavelength ($\lambda_{\mathrm{corr}} \sim N\lambda_{dB}$).

The dynamics of a completely condensed axion DF is governed by an equation of motion of Boltzmann-like form, and a Poisson equation for the mean field gravitational potential. The Boltzmann-like equation of motion in ASF1 is derived in a background FLRW cosmology. Here, we present the governing equations in non-moving Euclidean coordinates for simplicity. The step is simple

to reverse and there are no extrinsic changes to the Bose-specific physics. The large N limit are then

$$0 = \partial_t f^{(1)} + \boldsymbol{v}\cdot\nabla f^{(1)} - \nabla\Phi'\cdot\nabla_v f^{(1)} - \nabla\bar{\Phi}\cdot\nabla_v f^{(1)} - m_a\nabla_v\cdot\left(\int \mathrm{d}^6 w_2 f^{(1)}(w_2,t)\nabla\Phi_{12} \times \left(\frac{C-1-(\lambda_1+\lambda_2)f_+}{1+\lambda_2 f_+}\right) f^{(1)}(w_2,t)\right), \quad (3)$$

$$\nabla^2\bar{\Phi} = 4\pi G M\int \mathrm{d}^3 v f^{(1)}, \quad (4)$$

where G is the Newtonian gravitational constant, m_a is the axion mass, M is the total system mass, and we have dropped the gravitational potential from non-axion or non-condensed species. The non-axion species have been added to the Boltzmann-like equation in the canonical way. The gravitational potential of the non-axion species in general is governed by their own Poisson equation. $\bar{\Phi}$ is the single-body averaged Newtonian gravitational potential from axions, and Φ_{12} is the interaxion gravitational kernel

$$\Phi_{12} = \phi(\boldsymbol{x}_1,\boldsymbol{x}_2) = -\frac{G}{|\boldsymbol{x}_1-\boldsymbol{x}_2|}. \quad (5)$$

The Lagrange multipliers λ_1 and λ_2 of the interaxion correlation function are set by the normalization constraints on the single-body DF and the correlation function. The constraints are encapsulated by the single expression

$$1 = \int \mathrm{d}^6 w_1 f^{(1)}(w_1,t)\frac{C-\lambda_1 f_+}{1+\lambda_2 f_+}, \quad (6)$$

which is a function over phase space w_2 through f_+. Lastly, it is convenient in the equation of motion to replace the multiplier λ_1 with $\lambda_+ = \lambda_1 + \lambda_2$. The (λ_+, λ_2) pair will be the normal convention for the remaining sections. We refer to the Bose-specific dynamical contribution as exchange-correlation (XC) dynamics since they exist due to the enforcement of the exact Bose particle exchange symmetry and interaxion correlation from self-gravity. The collection of equations (3), (4), and (6) is the starting point for constructing the axion N-body algorithm. Recall that one regains the usual uncorrelated MFT case, meaning that the correlation function becomes unity, for $C = 1$.

3 GAINING INTUITION FOR AXION COLLAPSE WITH SPHERICAL SHELLS

Reducing the dimension of the full phase-space problem of equations (3), (4), and (6) to one may help to build an intuitive understanding of the physics involved. This subsection explores the collapse of angularly rigid spherical shells in both the static and rotational cases.

3.1 Spherical shell

This example is largely similar to the demonstration of Lentz et al. (2020). A thin and cold spherical shell of axions may collapse under its own gravity. For simplicity, we have additionally assumed no tangential axion motion about the centre that the radial velocity dispersion is sufficiently small so as to leave the shell thickness unchanged over the collapse. These assumptions reduce the dimensionality of the problem from 7 to 1. We also use constraints of $C = 1$, and $|\lambda_2 f_+| \ll 1$ to simplify the contribution of exchange–correlation interactions. Finally, λ_+ is taken as a free

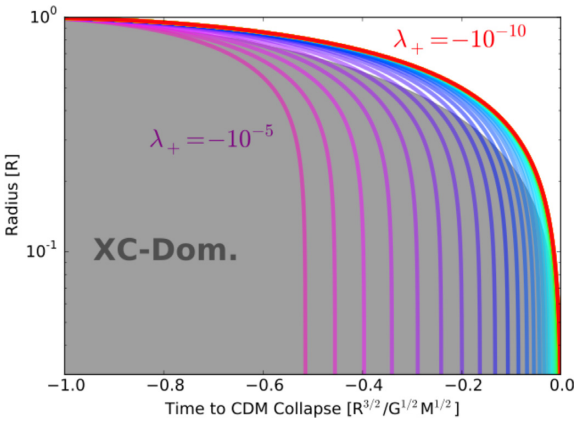

Figure 2. Collapse time to radius of spherical collapse from rest. The colour hue is logarithmic in λ_+, running from $\lambda_+ = -10^{-10}$ (red) at the top to $\lambda_+ = -10^{-5}$ (violet) at the bottom. The region where post-Newtonian physics dominates over classical gravity is shaded in grey. Adapted from Lentz et al. (2020). A colour version is available online.

tunable parameter for the purpose of demonstrating the range of effects from XC interactions. The governing equation of the Bose collapse may then be written to leading order in dispersion as

$$\ddot{r} = -\frac{GM}{r_{\rm soft}^2} + \lambda_+\left(\frac{3GMN(r_{\rm soft})}{4r_{\rm soft}^2} - \frac{GMN'(r_{\rm soft})}{4r_{\rm soft}}\right), \quad (7)$$

where M is the effective gravitating mass, $N(r_{\rm soft})$ is defined by

$$N(r_{\rm soft}) = \frac{1}{8\pi^2 r_{\rm soft}^2\sigma_r\sigma_v}, \quad (8)$$

where $r_{\rm soft}^2 = (r^2+\sigma_r^2)$, σ_r is the thickness of the shell, σ_v is the velocity dispersion of the shell and is held sufficiently small as to leave the shell thickness unchanged over the collapse. Note that the effective repulsion from the second two terms in the post-Newtonian contribution will never dominate over the first. Solutions of this system show that infall is amplified for non-trivial post-Newtonian contributions, Fig. 2. The new physics leads to a characteristically more violent infall due to the sharper form of the $\sim 1/r_{\rm soft}^4$ central XC force. Parameters chosen for spherical collapse are $r(t=0) = 1$, $\sigma_r = 10^{-3}$, and $\sigma_v = 10^{-4}$ in dynamical units.

The enhancement of Bose infall from XC falls in line with the general viewpoints on Bose enhancement: that identical bosons are increasingly attracted to regions of high boson density. Halo formation of Bose DM may be intuited to occur more quickly than CDM. New density profiles may also be expected from a more violent collapse.

3.2 Rotating spherical shell

Spinning the spherical shell about a central axis introduces the angular momentum pseudo-potential barrier into the system. The equation of motion for the shell is then

$$\ddot{r} = -\frac{GM}{r_{\rm soft}^2} + \frac{4L^2}{3\pi r_{\rm soft}^3} + \lambda_+\left(\frac{3GMN(r_{\rm soft})}{4r_{\rm soft}^2} - \frac{GMN'(r_{\rm soft})}{4r_{\rm soft}}\right), \quad (9)$$

where $L = M\omega R^2$ is the angular momentum of the respective cylinder of radius R. Normalization and other factors are kept the same as in the non-rotating case.

The presence of three singular forces allows for several possibilities in dynamics (Fig. 3). The angular momentum pseudo-

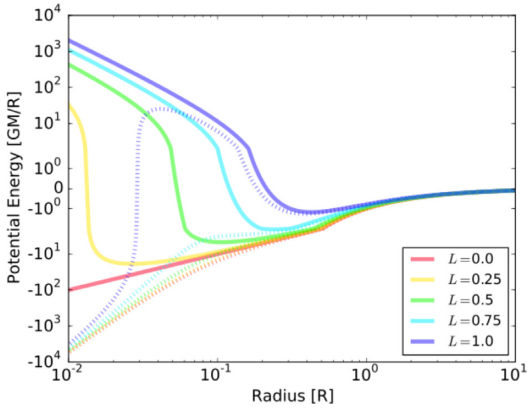

Figure 3. Pseudo-potential of rotating spherical shell versus radius. Solid lines correspond to classical infall, dashed lines to Bose infall at $\lambda_+ = -10^{-7}$. Angular momentum L of the shell is in units of $R^2\omega M^{1/2}/G^{1/2}$. Kinks seen in lines are artefacts of the symmetrical log scaling of the vertical axis and are not features of the potentials.

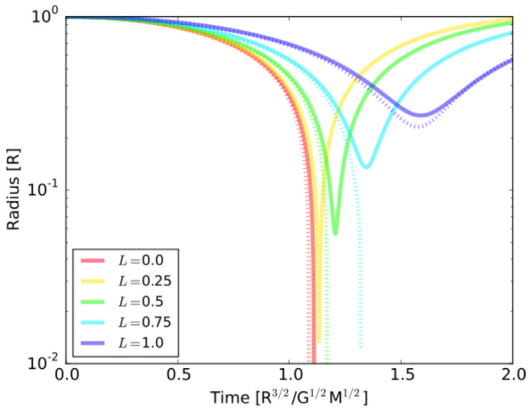

Figure 4. Trajectories of rotating spherical shell collapse versus time. Solid lines correspond to classical physics, dashed lines to Bose physics at $\lambda_+ = -10^{-7}$. Angular momentum L of shell is in units of $R^2\omega M^{1/2}/G^{1/2}$. Bose trajectories without rebound are physical as the Bose attractor has sufficiently degraded the angular momentum singularity.

potential is singular, repulsive and of scaling $\sim 1/r_{\rm soft}^2$, compared to the attractive $\sim 1/r_{\rm soft}$ classical gravitational attraction, and the $\sim 1/r_{\rm soft}^3$ Bose attraction, producing an island between the classical-dominated and Bose-dominated regions. The rotational island produces a region of relatively slowed motion, but for small L the angular momentum barrier is overcome and the collapse to singularity continues (Fig. 4). An unstable stationary point exists when the barrier equals the shell's initial energy. Higher rotation re-establishes the classical turn-around. As expected, there are accelerations in the rate, and increases in the depth, of Bose collapse.

The degradation of the angular momentum barrier provides further evidence that the accretion of a single condensate on to a Bose halo occurs more quickly than CDM, and may alter the haloes' shape and density profiles. The accretion of substructure and the process of major mergers may also be significantly altered by the sharply scaling extra-classical force. All that said, however, these heavily simplified one-dimensional models are no substitute for a full phase space numerical simulation.

4 *N*-BODY AXIONS

An efficient numerical algorithm reduces all continuum features of the axion model into discrete, well-ordered algebraic steps. The algorithm chosen for this paper is a combination of the MOC and leapfrog integration. MOC is a technique of discretizing over the space-like dimensions of the hyperbolic Boltzmann-like equation orthogonal to the time direction, here represented by phase space, by which we parametrize the characteristic curves of the solving DF (Courant & Hilbert 1953). The leapfrog method is used to integrate over the remaining time-like direction in a way that is stable to integrals of the motion (Ruth 1983). Derivations are restricted to purely condensed axion DM, free from state diffusion. A detailed derivation of the algorithm may be found in Appendix A. We assume here no interactions outside of self-gravity.

The algorithm first breaks down the spatial dimensions into a set of dynamic Lagrangian sample points, evolving through time via Hamilton-like equations, each of the form

$$\dot{f}_1 = 0, \tag{10}$$

$$\dot{\boldsymbol{x}} = \boldsymbol{v}, \tag{11}$$

$$\dot{\boldsymbol{v}} = -\nabla\bar{\Phi} - m_a \frac{\partial}{\partial\nabla_v f_1}\int \mathrm{d}^6 w_2 \nabla\Phi_{12} \cdot\nabla_v\left(f_1\frac{C-1-\lambda_+ f_+}{1+\lambda_2 f_+}f_2\right), \tag{12}$$

where f_1 and f_2 are the single-body DFs over phase spaces w_1 and w_2, respectively, and $\partial/(\partial\nabla_v f_1)$ is a functional derivative. Each sample can naturally be represented by the mass fraction m enclosed within its volume in phase space. The action of the functional derivative evaluates to

$$\begin{aligned}\frac{\partial}{\partial\nabla_v f_1}\int \mathrm{d}^6 w_2\nabla\Phi_{12}\cdot\nabla_v\left(f_1\frac{C-1-\lambda_+ f_+}{1+\lambda_2 f_+}f_2\right)&\\ = \int \mathrm{d}^6 w_2\nabla\Phi_{12}\left(\frac{C-1-\lambda_+ f_+}{1+\lambda_2 f_+}f_2\right)&\\ + \int \mathrm{d}^6 w_2\nabla\Phi_{12}\left(f_1\frac{-\lambda_+/2}{1+\lambda_2 f_+}f_2\right)&\\ - \int \mathrm{d}^6 w_2\nabla\Phi_{12}\left(f_1\frac{\lambda_2/2(C-1-\lambda_+ f_+)}{(1+\lambda_2 f_+)^2}f_2\right).&\end{aligned} \tag{13}$$

The resemblance of the equations on sample points to classical particle motion is striking, with the extra-classical terms appearing as additional forces acting upon the Bose 'particles'. Sample particles' equations of motion are accurate to the precision that the forces are known.

The second step of the algorithm integrates the sample points over time by discretizing the continuous time progression into an algebraic sequence. Over a single period of time $T = [0, t]$, the leapfrog method has three operations, often referred to as 'drift-kick-drift', to calculate a sample's next phase space configuration

$$\boldsymbol{x}(t/2) = \boldsymbol{x}(0) + \boldsymbol{v}(0)\frac{t}{2}, \tag{14}$$

$$\boldsymbol{v}(t) = \boldsymbol{v}(0) + t\left(-\nabla\bar{\Phi} - m_{\rm a}\frac{\partial}{\partial\nabla_v f}\int \mathrm{d}^6 w_2\nabla\Phi_{12} \cdot\nabla_v\left(f_1\frac{C-1-\lambda_+ f_+}{1+\lambda_2 f_+}f_2\right)\right)\Big|_{\boldsymbol{x}(t/2)}, \tag{15}$$

$$\boldsymbol{x}(t) = \boldsymbol{x}(t/2) + \boldsymbol{v}(t)\frac{t}{2}, \tag{16}$$

where the compact functional derivative form is kept for convenience. It is fortunate that the canonical form of leapfrog can be used despite the general velocity dependence of the XC force. The integration scheme is second order in time accuracy; however, the algorithm's symplectic nature does improve the long-term accuracy and stability of quantities such as energy and angular momentum, even relative to many higher order methods.

Calculation of the self-gravity can be performed in several ways. Once an optimal sampling choice has been made, which as well defines the sources of forces, an interpolation scheme of those forces can be constructed. Many efficient cosmology codes reduce the computational cost of gravity by differentiating between direct and long-range calculations of the classical gravitational potential, and simplifying the long-range calculations. This decomposition is often implemented on either a background mesh or a tree decomposition of particles. These interpolating techniques are capable of reducing the $O(n^2)$ scaling of direct two-body force calculation to a far more manageable $O(n\log n)$, or possibly in some cases even to $O(n)$ (Dehnen 2014), where n is the number of DF samples. Exchange–correlation interactions can be incorporated in the force calculation for Bose fluids. Fortunately, the XC interactions can be interpolated similarly to Newtonian gravity with several common techniques, for instance a tree decomposition, and preserve the scaling with particle number. Additional computational costs of the XC calculations are initially estimated at ∼50 per cent of the Newtonian gravity calculations. Other methods for gravity calculation exist, some of which may be better able to resolve the fine structure of DM haloes (Hahn & Angulo 2016; Sousbie & Colombi 2016; Colombi & Alard 2017). It remains to be seen whether XC forces can be integrated into these other methods.

5 CONDENSATE IN EXTERNAL POTENTIAL CODE

Developing a small-scale simulation code is important for testing the infall model. Fast turn-around allows for a quick development cycle. Further, a small platform is better able to keep pace with the developing theoretical work, discussed further in Section 9. Prior to implementing the above algorithms in one of the existing high-performance codes, we test them on a prototype platform, Condensate in eXternal Potential (CXP), to simulate isolated $3+1$D systems of interacting degenerate bosons in isolation, over a static cosmological background. The resultant algorithms for XC force integration are designed such that they, in principle, hold for a more complex implementation when calculated in parallel with the Newtonian gravity counterpart. Here, CXP is used to simulate the gravitational infall of near-spherical axion distributions through collapse and into virialization. The algorithms relevant to CXP are discussed below.

CXP utilizes the N-body and time-integration algorithms of Section 4 to simulate the phase-space evolution of self-gravitating bosons. The code is supplied with an initial distribution of sample points and the initial correlation C parameter. Sample points are quasi-randomly generated using a glass seed distribution (Baertschiger & Sylos Labini 2002), which is mirrored, randomly sampled, and re-scaled to fit the simulation parameters of particle number and distribution shape. Masses of each sample point and the initial correlation are propagated as integrals of the motion. Leapfrog evolution iterates over the Cauchy data, evolving it in time for a specified period.

The value of the XC Lagrange multiplier parameters need only be calculated at the initial distribution as the λs are also integrals of the motion. The constraint condition of equation (6) can be approximated via a mean-point integration

$$0=\sum_{i}^{n} w_i \frac{C-1-\lambda_+(f_i+f_2)/2}{1+\lambda_2(f_i+f_2)/2}, \tag{17}$$

where we have cancelled out the single DF integral to make the constraint condition null, and the w_i are partitions of the phase-space measure, or weights associated with each sample point. The weights play a similar role to the sample mass. Sample weights are taken to be equal across the distribution $w_i = w$, as are the masses of each sample point. One can find the unique solution to both multipliers by evaluating equation (17) at two unique points of the single body distribution, f_2. CXP uses f_2's maximum and minimum values as the two unique points.

Regarding the CXP implementation: the primary advantage of the highly parallelized routines, such as a tree decomposition, appear when used on large communications-limited networks, and are not of the same advantage for small n systems. CXP uses the direct $O(n^2)$ approach to interaction calculation, which provides developmental efficiency and agility.

For the interaction evaluation, using the Coulomb kernel for a particle's gravitational potential is not appropriate, as each 'particle' represents many axion quanta. Instead, a softened potential using the $K1$ profile of Dehnen (2001) is applied to each sample. $K1$ has the potential

$$\Phi^{K1}(\acute{r}) = \begin{cases} \frac{-G}{32\acute{r}}\left(64-105\acute{r}+175\acute{r}^3-147\acute{r}^5+45\acute{r}^7\right) & 0\le r'\le 1, \\ -G/\acute{r} & r'\ge 1, \end{cases} \tag{18}$$

where $\acute{r}=r/d$, d is the characteristic softening length, and the kernel mass is set to unity. Note that for Bose systems simulated for lengths beyond the de Broglie scale, this softening length should match the expected level of smoothing to yield minimal force error and not simply some intrinsic particle scale (Dehnen 2001). The $K1$ kernel is chosen for its computational efficiency and spatially compact support. The $K1$ kernel does have the unusual characteristic of containing a spherically symmetric region of negative Poisson mass density. This does not imply that the DF becomes negative in an annulus about the sample, it is merely an alteration to the force profile. The softening length commensurate with the particle density is

$$d=\epsilon\left(\frac{4/3\pi R^3}{n}\right)^{1/3}, \tag{19}$$

where R is the characteristic radial length scale of the initial configuration, and ϵ is a numerical factor that fixes the softening length. The $K1$ profile is not ubiquitous among pure N-body codes, with some instead favouring a spline mass profile (Merritt 1996; Dehnen 2001), which we will study in future simulations.

The XC force is straightforward to calculate once the integral over phase space is performed (see Appendix A). Furthermore, the XC forces between two particles are central, and only dependent on the particles' positions, masses, and with sample DF values, so that both angular momentum and energy are conserved in a collisionless Bose system. The total force felt by an N-body

particle is

$$\boldsymbol{F}_1 = -\sum_i^n \nabla\Phi_{1i} - \sum_i^n \nabla\Phi_{1i}\left[\frac{C-1-\lambda_+(f_1+f_i)/2}{1+\lambda_2(f_1+f_i)/2}\right] - \sum_i^n \nabla\Phi_{1i}\left[\frac{-\lambda_+ f_1/2}{1+\lambda_2(f_1+f_i)/2}\right] + \sum_i^n \nabla\Phi_{1i}\left[f_1\frac{\lambda_2/2\,(C-1-\lambda_+(f_1+f_i)/2))}{(1+\lambda_2(f_1+f_i)/2)^2}\right], \quad (20)$$

where Φ_{1i} is the softened potential between samples at positions $\boldsymbol{x}_1$ and $\boldsymbol{x}_i$. CXP uses the same softening for XC as the mean Newtonian interaction. The first sum of equation (20) gives the mean Newtonian force, and the last three sums are XC terms. Recall that the sample DF value is integral along the characteristic curve through phase space, making the bracketed terms easily calculable when the initial DF value is propagated with the sample. This ease in computation obfuscates a subtle point, however, that for beyond-CXP computations the XC force can be velocity dependent. The terms in square brackets will be constant for a given particle pair because the phase space density is an integral of the motion in a purely condensed collisionless system. However, collisions or a change in the system's density of states would change the particles' phase space densities over time. In particular, collisions that change the velocity distribution will change the phase space density and hence introduce an implicit velocity dependence into the XC force on each particle. Mean Newtonian gravity would not respond to such changes. Our algorithm does not currently handle a dynamical density of states or collisional effects. Further discussion of the phase-space dependence of the XC force can be found in Appendix A.

Time-stepping is performed uniformly over the system. The leapfrog time-step size is chosen such that the fastest orbits contain multiple dozen steps per orbit so as to be well resolved at first shell crossing, even in the most violent of collapses. This requirement lowers the time-step to $\delta t \lesssim 10^{-2} t_{\rm dyn}$ for many of the presented simulations, where $t_{\rm dyn} = 1/\sqrt{GM/R^3}$ is the dynamical crossing time for a typical orbit of the uncorrelated system. The short time-step ensures adequate resolution of the fastest orbits in the system, but over-resolves the slower orbits. The code is currently parallelized over the interaction calculation at the single time-step level for both single-node CPU and GPU resources.

We choose the duration of the simulations to be long enough such that virialization is well established for much of the bound portions of the halo, but short compared to the two-body relaxation time-scale. The two-body relaxation time-scale is

$$t_{\rm relax} \approx \frac{0.1n}{ln(n)} t_{\rm cross}, \quad (21)$$

as derived in Binney & Tremaine (2008), where $t_{\rm cross}$ is the system crossing time, closely related to the dynamical time. The crossing time, in our case, is altered by the presence of additional forces, as is the form of the total force. We find the time to two-body relaxation, using an adjusted relaxation time to account for XC, to be of the order of many dozens to thousands of crossing times for systems of $n = 10^3$–10^5. Among the calculated outcomes, classical infall is naturally found to take the longest for fixed n as the XC force on average amplifies the experienced gravitational force, shortening the crossing time by an estimated 0.5 at $C = 0.5$. Only several dynamical times are required for a system to virialize, so a period of 10 dynamical times is chosen to preserve the details of infall.

6 THE SIMULATIONS

The collapse of spherical or near-spherical distributions is a productive first step in classifying the effects of self-gravity. Several configurations are tested here, including the cold homogeneous sphere, the Gaussian cold sphere, and configurations imparted with small solid-body spin. Simulations consist of 50 000 particles. The configurations sampled for the suite of simulations presented here take on the outer product of parameters of shape, correlation, and spin:

(i) Shape $\in$ {Top-hat, Gaussian}.
(ii) $C \in \{0.5, 0.75, 0.9, 1.0\}$.
(iii) $\lambda \in \{0.0, 0.05, 0.10\}$.

Individual simulations of this type will be referred to as S (shape, C, λ). CDM and Bose simulations share initial DFs.

6.1 Top-hat sphere

The most basic and most violent collapses available to pressure-less self-gravitating fluids occur with sphere initial conditions of homogeneous density and zero velocity (Gunn & Gott 1972). Density of the sphere is given by the normalized Top-hat distribution

$$\rho_{\rm TH} = \frac{3M}{4\pi R^3} H(R-r), \quad (22)$$

where R is the radius of the sphere surface, M is the total mass, and H is the Heaviside function. Giving the sphere a perfectly cold momentum distribution is tempting, but it leads to divergent values of the Lagrange multipliers and also leads to numerical artefacts. A normally distributed smoothing in velocity is therefore applied, with velocity dispersion being a small fraction of the crossing time $\sigma_v t_{\rm dyn} < 0.01R$. In the pressure-less fluid case, the cold homogeneous sphere ideally collapses, approaching a single point, before the drastic non-linearity of the singularity and spherical symmetry breaking inherent of the sampling scatters the distribution into a gentler configuration. Observing such severe collapses should provide a near-optimal probe of the XC contributions to the $1/R^3\sigma_v^3$ or $1/d^3 v_{\rm sng}^3$ scales in phase space, where $v_{\rm sng}$ is the speed at shell crossing. The time-step size is set at $\delta t = 0.5 \times 10^{-2} t_{\rm dyn}$ so as to adequately resolve the softened singularity. A softening length factor of $\epsilon = 2$ is used for stability of the resulting halo. These simulations, while interesting probes of the XC physics, do not map well to cosmological haloes and are therefore their results are deferred to Appendix B.

6.2 Gaussian sphere

A less violent and more cosmologically sensible example is the Gaussian sphere. Its density is given by an isotropic normal distribution

$$\rho_G = \frac{MR^3}{(2\pi)^3} e^{-r^2/(R^2/2)}, \quad (23)$$

where $R/2$ is the dispersion radius of the sphere. The Gaussian sphere shares its other qualities such as primordial velocity dispersion with the homogeneous sphere. A time-step of $\delta t = 0.5 \times 10^{-2} t_{\rm dyn}$ and a softening length factor of $\epsilon = 1$ are used for stability.

6.3 Spinning spheres

Angular momentum plays a significant role in the formation of structure in cosmology, and understanding the reaction of the XC

physics to angular momentum is important for building an intuitive picture of Bose infall. The Bose halo structure is not expected to be influenced by vortices, which are standard structures in rotating superfluids, as the physics of the vortex scale is suppressed with the de Broglie scale. Angular momentum, instead, is to be imparted to the particles as a solid-body spin about the centre of the sphere

$$\boldsymbol{v}_{\rm rot} = \omega\hat{\boldsymbol{z}} \times \boldsymbol{r}, \tag{24}$$

where ω is the angular speed, $\hat{\boldsymbol{z}}$ is a constant unit vector, and the multiplication operator is the three-dimensional cross product. The self-gravitating spin parameter of Peebles (1969) is used to calculate the angular velocity ω by evaluating the relative size of angular momentum to the overall energy contribution via

$$\lambda = \frac{J|E|^{1/2}}{GM^{5/2}}, \tag{25}$$

where J is the magnitude of the total angular momentum, E is the total binding energy, and M is the total mass of the distribution. The parameters of simulation are shape, correlation, and spin are then varied to study potential unique Bose structures.

7 RESULTS

The key result of this study is that the collection of spherical collapse simulations display a broad set of structural differences between Bose and classical infall. The observed Bose features fall into several categories, including alteration of formation history, creation of new broad substructures, violations of classical binding conditions, and new fine structure. This section focuses on a single thread of unique Bose structures from Gaussian simulations, stringing from initial collapse and virialization to observables crucial to operating axion DM direct detection searches. The reader interested in more detail concerning the following Bose structures for Gaussian and Top-hat simulations is encouraged to read Appendix B. Further signatures of Bose DM found in these simulations can be found in Appendix C. Convergence tests for the simulations can be found in Appendix D.

The first unique signatures of Bose infall can be seen during initial collapse and virialization. As the spherical shell demonstration implies, XC quickens the rate of first infall. Following the central distribution of mass over infall and virialization shows an increase in the rate of collapse to shell crossing by up to ∼20 per cent at $C = 0.5$, Fig. 5. The quickened rate of collapse also impacts the halo's violent relaxation phase, with the chaotic phase of Bose simulations being subdued and passing more quickly than their classical counterparts. The characteristic relaxation times are reduced by more than one dynamical time for Bose infall, from $T_{\rm rel} \approx 3t_{\rm dyn}$ for classical infall to $T_{\rm rel} \lesssim 2t_{\rm dyn}$ for Bose infall at $C = 0.5$. Halo spin seems to have only a weak effect on the features of collapse time, length of the chaotic phase, and resulting central mass.

Such an alteration in the formation history of the Bose halo may be expected to produce a significantly different equilibrium structure. The radial density profile, the standard global measure of halo structure, however displays little sensitivity to XC. Radial density profiles of Gaussian infall show a universal broken power law suggestive of the cosmologically universal shape of NFW (Navarro–Frenk–White) (Navarro, Eke & Frenk 1996a; Navarro, Frenk & White 1996b), Fig. 6. The haloes with static cosmological scale factor show a stee per central cusp of $\alpha \approx -1.7$, breaking slowly at $r_{scale} \sim 0.4R$ into an outer power law of $\beta \sim -2.8$. Some small changes in the density profiles that scale with correlation are seen at and beyond the virial radius, around ∼2–3R. The virial

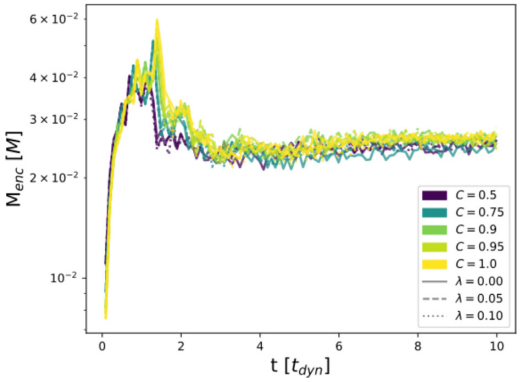

Figure 5. Mass within central $r = 0.05R$ of halo over time of Gaussian isolated collapse simulations of Section 6. Profile coloration indicates degree of correlation ranging from classical $C = 1.0$ to highly correlated $C = 0.5$. Line style indicates level of Peeble's spin λ of the halo. The time to collapse is seen to be shorter for correlated haloes, as is the time between first infall and virialization.

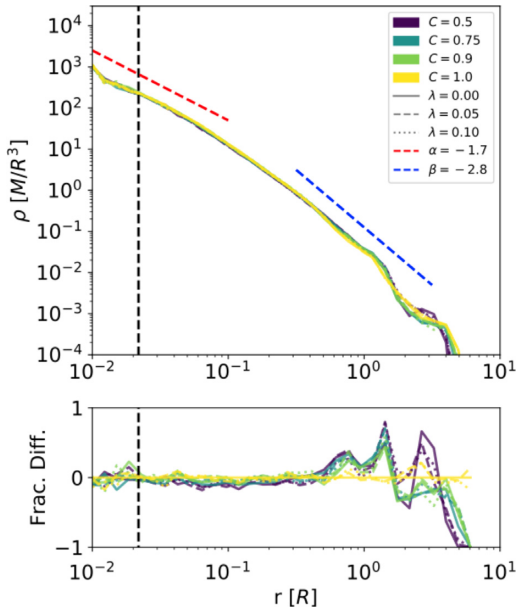

Figure 6. Mass density radial profiles of the Gaussian isolated collapse simulations of Section 6 after $10t_{\rm dyn}$. (Top) Raw measurements and (Bottom) fractional differences from the classical spin-less halo. Profile coloration indicates degree of correlation ranging from classical $C = 1.0$ to highly correlated $C = 0.5$. Line style indicates level of Peeble's spin λ of the halo. Comparison power laws are given for the inner (α) and outer (β) halo structure. The softening profile's maximum force radius is represented by the black dashed line in each simulation set, below which our confidence in the results is diminished.

radius is defined here to be the radius beyond which less than five crossing times have elapsed. The dependence of the breaking radius with spin is weak, much like in cosmological CDM. No significant new structure in the form of a central core or other features is seen for Bose Gaussian collapse, even reproducing the emergent scale radius of the classical haloes. This insensitivity to correlation is surprising, as XC forces would be expected to be significant for highly correlated condensates.

The XC physics is found to make an impact on the phase-space density. The mean phase-space density profiles show consolidated

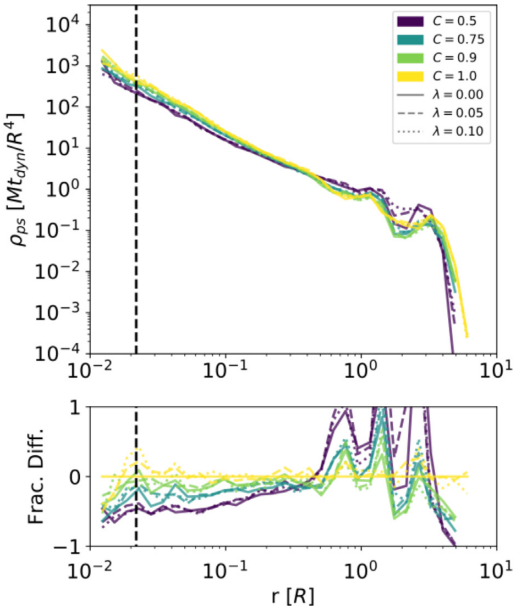

Figure 7. Phase-space mass density radial profiles of the Gaussian isolated collapse simulations of Section 6. (Top) Raw measurements, (Bottom) fractional differences from the classical spin-less halo. Haloes were measured after evolving for $10t_{\rm dyn}$. Profile coloration indicates degree of correlation ranging from classical $C = 1.0$ to highly correlated $C = 0.5$. Line style indicates level of Peeble's spin λ of the halo. Volume in velocity space is measured in the local spherical velocity dispersion. The softening profile's maximum force radius is shown by the black dashed line in each simulation set, below which our confidence in the results is diminished.

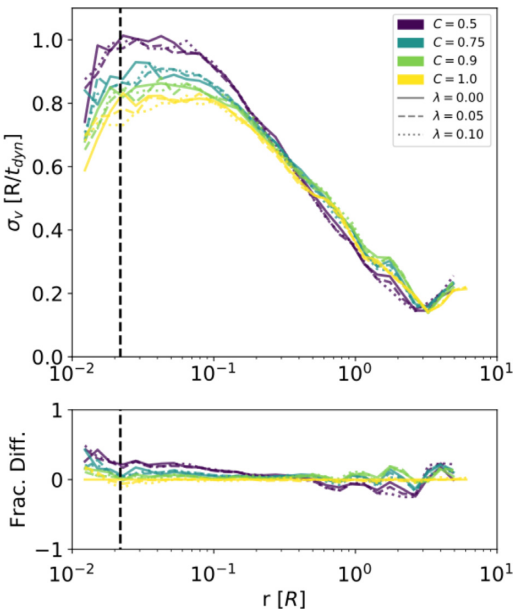

Figure 8. Spherical velocity dispersion radial profiles of the Gaussian isolated collapse simulations of Section 6 after $10t_{\rm dyn}$. (Top) Raw measurements, (Bottom) fractional differences from the classical spin-less halo. Profile coloration indicates degree of correlation ranging from classical $C = 1.0$ to highly correlated $C = 0.5$. Line style indicates level of Peeble's spin λ of the halo. The softening profile's maximum force radius is shown by the black dashed line in each simulation set, below which our confidence in the results is diminished.

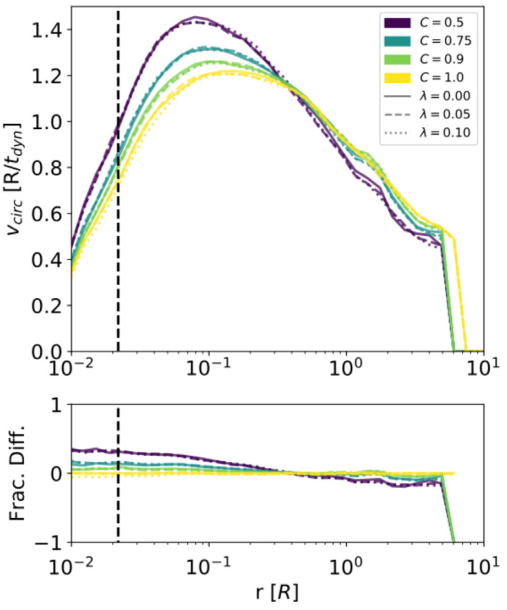

Figure 9. Circular orbit speed radial profiles of the Gaussian isolated collapse simulations of Section 6 after $10t_{\rm dyn}$. (Top) Raw measurements and (Bottom) fractional differences from the classical spin-less halo. Profile coloration indicates degree of correlation ranging from classical $C = 1.0$ to highly correlated $C = 0.5$. Line style indicates level of Peeble's spin λ of the halo. The softening profile's maximum force radius is shown by the black dashed line in each simulation set, below which our confidence in the results are diminished.

shifts with correlation ranging from the inner halo to the outermost back-splash shells (Fig. 7). The relative invariance of the spatial density profiles attributes this change wholly to the large differences in velocity dispersion (Fig. 8). The intersection radius between the Bose and classical haloes in both the phase-space and velocity dispersion profiles is the same as the density profile scale radius. The increased velocity dispersion also increases the classical virialization ratio.

The XC force is responsible for containing Bose DM in a halo of the same shape as CDM despite its enhanced speed. Circular orbit speed profiles show how the experienced force-per-particle differs in the virialized haloes (Fig. 9). Circular velocities of classical haloes build quickly in the inner halo, where densities are large, and recede in the outer halo where mass is depleted. This characterization is amplified for Bose haloes, where the high-density regions are also a source of large XC force, which is aligned with classical gravity, and low-density regions that produce anti-aligned XC forces. The XC is seen to cause an amplification of circular speed by almost 50 per cent at halo centre, corresponding to a doubling of force, and 20 per cent at peak force, or 40 per cent increase in force, relative to classical. Somewhat lower reductions in net force are seen in the outer halo. Note that the transition point between amplification and reduction is again the density profile's scaling radius.

The explicit structure of the velocity distribution reveals further signatures of Bose physics. The distribution of speed as a fraction of classical binding limit $v_{\rm max} = \sqrt{2\bar{\Phi}}$ shows new macroscopic structure at high speeds, Fig. 10. The classical haloes' speed distributions show a single thermal-like peak at $v/v_{\rm max} \approx 0.25$ followed by a tail that becomes truncated at $v/v_{\rm max} \approx 0.8$. Bose haloes show a more columnated distribution with a second peak appearing at the high-speed end of the distribution. The double-lobed plateau of the Bose distributions is a major departure from

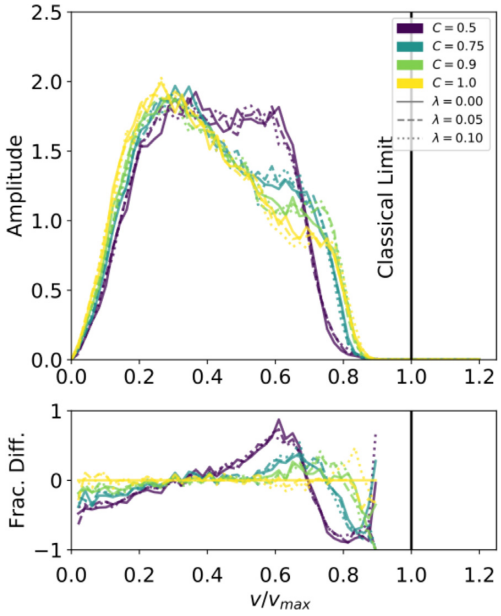

Figure 10. DFs of speed fraction over classical gravitational potential $v/v_{\max} = v/\sqrt{2|\bar{\Phi}|}$ of Gaussian isolated collapse simulations of Section 6. Gaussian profiles on L, Top-hat profiles on R. Haloes were measured after evolving for $10t_{\rm dyn}$. Distributions are taken from within the scale radius $r = 0.4R$ for Gaussian simulations and $r = 1.0R$ for Top-hat. Profile coloration indicates degree of correlation ranging from classical $C = 1.0$ to highly correlated $C = 0.5$. Line style indicates level of Peeble's spin λ of the halo. Sample points lying outside of the classical limit occur only with haloes of correlation $C = 0.75$ or stronger, and amount to about one tenth of a per cent of the sampled mass.

the classical halo and imply a marked change in the energy macro-structure of Bose haloes. Distribution centres of mass are weakly dependent on correlation, staying close to $\langle v/v_{\max}\rangle \approx 0.4$.

Bose infall also impacts the fine structure of the DM halo. The radial orbital action, namely the Fourier transform of a particle's displacement from the halo centre, carries with it several of the halo's fine phase-space structures and other non-thermal features. A probability distribution constructed from the particles' radial actions over mean orbit radius shows multiple phase-space structures with XC dependence (Fig. 11). For instance, from the prominent branch peaking at $\bar{r} \sim 1R$, one counts 10 distinct branches in the provided classical halo. The other Gaussian haloes are provided in Appendix C. Noise and force softening obscure these structures below $\bar{r} = 0.04R$. The correlated Bose haloes present many more branches over the same range, reaching 16 for the provided halo at $C = 0.5$, becoming crowded to the point of large overlap with mean orbit radius.

Bose structures both fine and gross may be visible to current and future axion DM searches. For instance, direct detection axion DM experiments such as ADMX, HAYSTAC, and others (Brun et al. 2017; Du et al. 2018; Jeong et al. 2018; Zhong et al. 2018), are capable resolving fine details of the local axion energy distribution, down to a part in 10^{12} of the rest-mass energy. Unique Bose structures are visible in energy distribution measures for an estimated direct detection experiment at the solar radius (Fig. 12). The primary visible Bose feature is the high speed excess seen in Fig. 10. The thermal peak of the classical halo is seen to be depleted relative to the width of the distribution in favour of a second high-energy peak at K.E. $= 4GM/R$. In the halo centred frame, the two peaks come close to inverting in prominence for $C = 0.5$ and may be observed to do so for the extreme correlation case of $C = 0.0$. The circularly orbiting frame measurement disperses the high-energy peak, though the thermal depletion is still quite visible. The local measurement is not well resolved enough to pick up the altered branching phase space structure or other fine structures.

8 DISCUSSION

We now seek to further classify the differences in structure observed between Bose and classical haloes. Determining the sources of new structure will be a continuing process going forward as simulations and techniques become more sophisticated.

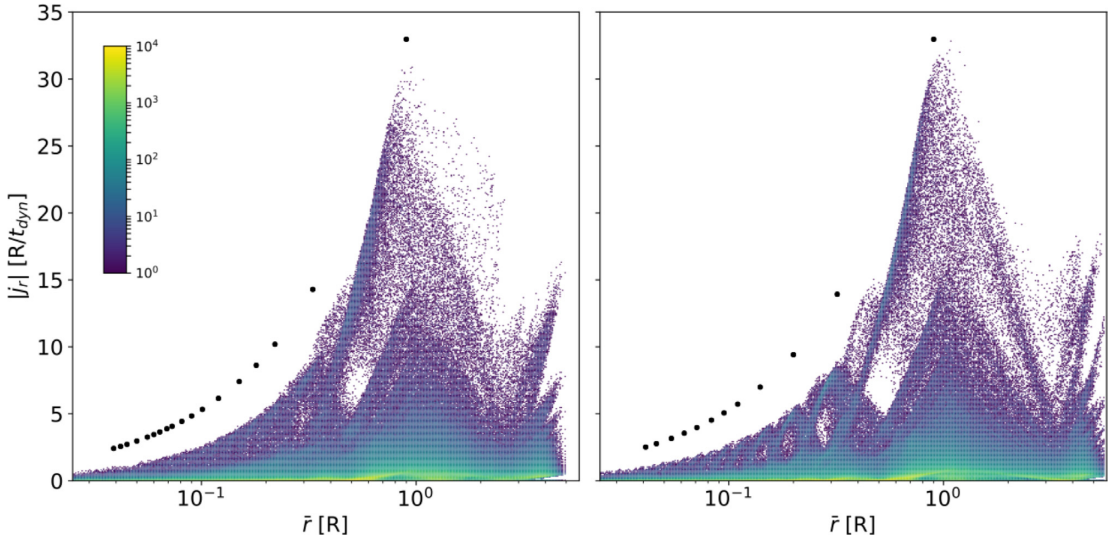

Figure 11. Radial orbital action and mean orbit radius distributions of Gaussian isolated collapse simulations. (Left) The Bose halo from simulation *S* (Gaussian, 0.5, 0.05). (Right) The classical halo from simulation *S* (Gaussian, 1.0, 0.05). Samples are taken from 100 equally spaced frames during 10–$12t_{\rm dyn}$. Sample points are taken such that each particle is given one mean radius and the radial autocorrelation power spectrum. Locations of fine structural peaks are indicated by black dots. See also Fig. B8.

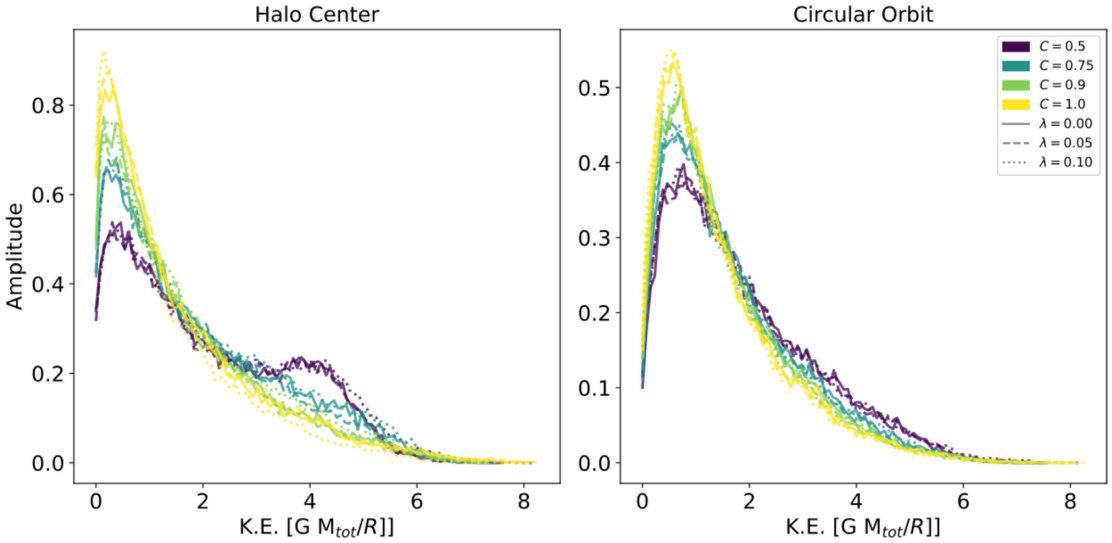

Figure 12. Kinetic energy spectra of Gaussian isolated collapse simulations. Samples are taken from stacked time-slices of simulations of post-virialized haloes, explained in Section C3. Samples are taken from a toroid of extent $0.04R \leq s \leq 0.06R$ and $-0.01R \leq z \leq 0.01R$ in cylindrical coordinates. The origin of the coordinate system is placed at the halo centre, and the orientation has $\hat{\boldsymbol{z}}$ is parallel with $\boldsymbol{j}_\phi$. Kinetic energies are measured (Left) from a halo-centred frame of reference, or (Right) a frame on circular orbit at radius $s = 0.05R$ that is co-moving with the halo's net spin. The co-moving frame is an analogue to the Sun's motion in the Milky Way halo. Note the distinct Bose-related structure at (Left) about energy K.E. $= 4GM/R$.

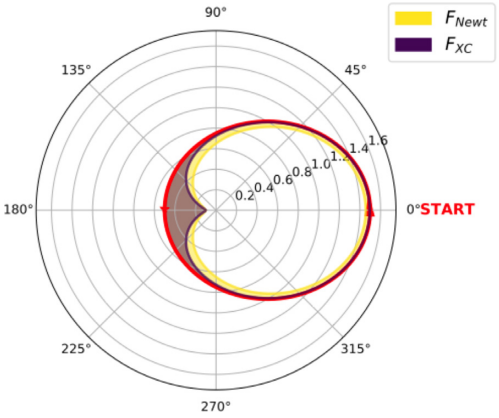

Figure 13. Illustration of the force experienced by a test DM particle in a spherically symmetric Bose halo with density profile similar to that in the Top-hat simulations. The angle is the one canonical to the radial action. The forces extend radially from the orbit point towards the plot centre. The classical Newtonian force (yellow) is periodic with maximum at the point of closest approach. The XC force (purple) varies more widely with radius, as the average phase-space density increases towards the centre of the halo. Note that this orbit would not be closed, in general. A colour version is available online.

The initial infall of halo progenitors produces the expected result of lessening the time to, and increasing the speed of first shell crossing, as predicted by the example of in-falling spherical shells in LQR and Section 3. Gaussian haloes show a quickening of infall of the order of $O(30\sqrt{1-C})$ per cent. Top-hat haloes widen that quickening. An earlier infall would shift slightly the formation of early galaxies and other large structures to earlier cosmological times. Observational evidence and numerical models of early halo formation, through the epoch of reionization for example, currently do not favour such an outcome (Mesinger 2016). The shift is only slight, fortunately, and not likely to have much of an effect on the redshift of re-ionization. Faster crossing times and other properties of the XC force also leads to shorter times to virialization. Rate of equilibration among Gaussian Bose haloes is seen to increase relative to classical haloes by $\sim 70(1-C)$ per cent. The briefer time to form a stable halo may notably change the formation history of the first stars as the neutral gas cooling rate is highly sensitive to the halo's potential well.

Fluid elements of Bose DM are subject to forces larger than that of Newtonian gravity at the halo centre and weaker than at the halo's edge. Variance in force in Gaussian haloes orders well with velocity dispersion variation of those same haloes. In the presence of near-identical spatial distributions, we consider the change of force variation throughout a halo as evidence of effective velocity dependence in the XC interaction. Further, there may be an opportunity to observe this force variation via the sub-structure of major haloes. If it is found that the matter in haloes and their sub-structure remain correlated to one another, it is possible that the forces experienced by the Bose DM sub-structure, such as satellite galaxies, are also altered relative to the classical case. The gravity felt by baryons within a satellite galaxy would be dominated by the Newtonian potential and, being bound to the sub-halo, would be pulled along the modified orbit. The possible implications for sub-structure orbits and their organization will be actively pursued in future cosmological simulations.

The similarity of virialized density and anisotropy profiles among Bose and classical haloes is unexpected. The shown difference in force and dependence of XC on the full phase-space density provide multiple opportunities for a halo to settle into a differently shaped state. Put another way, there appear to be mechanisms that one would expect to force the halo into a new configuration. For example, the XC force experienced by particles on highly radial trajectories is significantly different than the Newtonian force, Fig. 13, implying that each halo would have very different orbital structures. The orbital analysis of the previous section did show a sizable change in both the number and size of orbital fine structures within the virial volume. Though, again, the influence

of these structures appears to be limited to the overall kinematics as there are no observed large-scale deviations of halo spatial structure from the universal profile. A more precise investigation of a Bose halo's orbital properties, and how these properties play into reproducing the emergent scales of classical haloes, will be left for future work. It is also worth noting that constraint forces perform no work, making a part of the XC's ability to transport energy through the distribution limited. Appendix 3 provides some further insight on the altered force profile for spherical shell collapse.

The role of the breaking radius $r_{\rm scale} = 0.4R$ in the Gaussian density profile is itself an interesting topic. The breaking radius is found to be insensitive to both spin and correlation, see Fig. 6. Many kinematical and dynamical transitions between classical and Bose haloes also occur at this radius, such as the behaviour of mean phase-space density, spherical velocity dispersion, circular velocity curve, and others, see Figs 7, 8, 9, and Appendix C. This consistency of emergent scales may be indicative of significant underlying physical phenomena important to both classical and Bose haloes.

Changes to structure, even at the present level of coarse graining, presents windows to detection of the axion. The observed kinematical signatures of Bose physics such as variations of circular orbit speeds, enhanced velocity dispersion, and migration of the fractional speed distribution are all potentially visible in direct and indirect axion detection efforts (Lentz et al. 2017; Bull et al. 2018; Foster, Rodd & Safdi 2018; Knirck et al. 2018; more on this).

9 SUMMARY

This paper extends the analysis of the highly correlated QCD axion DM of Lentz et al. (2019) into the non-linear regime of structure formation. The Boltzmann-like equation derived in Lentz et al. (2019) governing the dynamics of a degenerate correlated Bose fluid is first re-introduced, and the significance of XC interactions is reviewed. The numerical algorithms for an *N*-body simulation are obtained from the continuum equation of motion by using the MOC, discretizing the continuum DF into sample points whose individual equations of motion are seen to be different from that of standard Newtonian gravity.

Simulations of spherical and rotating collapse are examined in a static cosmology using the small-scale *N*-body solver 'Condensate in eXternal Potential'. Comparisons between Bose physics and the standard pressure-less cold DM model show unique Bose structures during initial infall, chaotic relaxation, and persisting into virialization. Novel Bose structures are found to include:

(i) Significantly augmented forces on DM fluid elements.

(ii) Quickening of first infall by $\gtrsim 30\sqrt{1-C}$ per cent and faster rates of equilibration by $\gtrsim 60(1-C)$ per cent.

(iii) Altered orbital characteristics of DM, including increases and decreases in circular orbit speed by $\gtrsim 130(1-C)$ per cent.

(iv) New macroscopic populations at moderate to high energy or speed relative to classical limits.

(v) New and increasingly self-similar orbital phase space structures and other fine structures.

(vi) Convergence of the universal emergent scale in the halo mass-density profile with Bose kinematical and dynamical transition scales from greater-than-classical to less-than-classical.

(vii) Notable *lack* of effects on the halo density and anisotropy profiles.

The above novel structures already suggest several observables for searches among direct and indirect axion DM experiments, and in the observation of DM effects on baryonic processes.

The presence of surviving Bose-specific structures in simulations is a significant development in the search for DM. The presented small-scale simulations are far from sufficient to identify all possible Bose structures, however. Higher resolution, the incorporation of baryons, and the use of cosmologically motivated initial conditions are needed to better understand the structural differences of a Bose fluid in a realistic and cosmological environment. A natural development is to build on the small-scale tests of the generalized Bose condensate dynamics, incorporating them into the highly sophisticated *N*-body + Smoothed-Particle-Hydrodynamics code, such as CHANGA (Menon et al. 2015). Increasing resolution and incorporating in well-modelled non-DM species in a cosmological setting will provide further insight into the fuller extent of unique axion DM structures.

Lastly, there are two fundamental challenges to address in order to create a realistic physically motivated model of axion structure formation. First, adding baryonic species to a system of highly degenerate bosons influences not only the classical gravitational potential of that system, but may also alter the fraction of bosons in the condensate. The derivations of ASF1 are made in the environment of minimal baryonic gravity. This condition may not necessarily be satisfied near the centres of galaxies, where baryonic densities greatly exceed those of DM. Specifically, the addition of a significant non-Bose gravitating species disrupts the symmetry used to solve the many-body Schrödinger equation of Lentz et al. (2019), a symmetry which permitted condensate solutions as products of two-body correlators. External potentials can therefore introduce a migration of states in the highly degenerate fluid, meaning the complete-condensate formalism may not hold in a realistic cosmological context. The effective size of those influences on the correlation is a topic of ongoing research.

Secondly, it is not obvious how much correlation exists within these systems of axions at the start of the collapse, that is, the value of *C*. Initial correlation has so far been a tune-able integral parameter treated as not specified by the physics. A great deal of physics and different dynamical regimes occur between the epoch of the parent pseudo-scalar field appearance and post-recombination structure formation. A complete description of state dynamics within and outside of the degenerate state of DM axions, from the well-motivated conditions of the pre-inflation era to the matter era, is also a topic of current study. A dynamical description of state tracking will help resolve the extent to which the Bose physics of mixed condensed and non-condensed states can create structure unique from that of standard CDM, and is a topic of future work.

ACKNOWLEDGEMENTS

We would like to thank Jens Niemeyer, Katy Clough, David Marsh, Bodo Schwabe, Jan Velmatt, Xiaolong Du, Marcel Pawlowski, and Ewald Puchwein for their productive discussions. We also gratefully acknowledge the support of the U.S. Department of Energy Office of High Energy Physics and the National Science Foundation. TQ was supported in part by the NSF grant AST-1514868. EL and LR were supported in part by the DOE grant DE-SC0011665.

REFERENCES

Angulo R. E., Springel V., White S. D. M., Jenkins A., Baugh C. M., Frenk C. S., 2012, MNRAS, 426, 2046
Baertschiger T., Sylos Labini F., 2002, Europhys. Lett., 57, 322
Banik N., Sikivie P., 2016, Phys. Rev. D, 93, 103509
Barnes J., Hut P., Goodman J., 1986, ApJ, 300, 112
Bellovary J. M., Dalcanton J. J., Babul A., Quinn T. R., Maas R. W., Austin C. G., Williams L. L. R., Barnes E. I., 2008, ApJ, 685, 739
Berges J., Jaeckel J., 2015, Phys. Rev. D, 91, 025020
Binney J., Tremaine S., 2008, Galactic Dynamics, 2nd edn. Princeton Univ. Press, Princeton
Brun P. et al., 2019, EPJ C, 79, 186
Bull P. et al., 2020, PASA, 37, e002
Bullock J. S., Dekel A., Kolatt T. S., Kravtsov A. V., Klypin A. A., Porciani C., Primack J. R., 2001, ApJ, 555, 240
Colombi S., Alard C., 2017, J. Plasma Phys., 83, 705830302
Courant R., Hilbert D., 1953, Methods of Mathematical Physics. Interscience Publ., New York
Davidson S., 2015, Astropart. Phys., 65, 101
Dehnen W., 2001, MNRAS, 324, 273
Dehnen W., 2014, Comput. Astrophys. Cosmol., 1, 1
Dehnen W., Read J. I., 2011, Eur. Phys. J. Plus, 126, 55
Diemand J., Moore B., Stadel J., 2005, Nature, 433, 389
Du N. et al., 2018, Phys. Rev. Lett., 120, 151301
Erken O., Sikivie P., Tam H., Yang Q., 2012, Phys. Rev. D, 85, 063520
Foster J. W., Rodd N. L., Safdi B. R., 2018, Phys. Rev. D, 97, 123006
Gunn J. E., Gott J. R., III, 1972, ApJ, 176, 1
Guth A. H., Hertzberg M. P., Prescod-Weinstein C., 2015, Phys. Rev. D, 92, 103513
Hahn O., Angulo R. E., 2016, MNRAS, 455, 1115
Jeong J., Youn S., Ahn S., Kim J. E., Semertzidis Y. K., 2018, Phys. Lett. B, 777, 412
Kelley K., Quinn P. J., 2017, ApJ, 845, L4
Knirck S., Millar A. J., O'Hare C. A. J., Redondo J., Steffen F. D., 2018, J. Cosmol. Astro-Part. Phys., 2018, 051
Leggett A. J., 2006, Quantum Liquids: Bose Condensation and Cooper Pairing in Condensed-Matter Systems. Oxford Univ. Press, Oxford
Lentz E. W., Quinn T. R., Rosenberg L. J., 2016, ApJ, 822, 89
Lentz E. W., Quinn T. R., Rosenberg L. J., Tremmel M. J., 2017, ApJ, 845, 121
Lentz E. W., Quinn T. R., Rosenberg L. J., 2019, MNRAS, 485, 1809
Lentz E. W., Quinn T. R., Rosenberg L. J., 2020, Nucl. Phys. B, 114937
Mansfield P., Kravtsov A. V., Diemer B., 2017, ApJ, 841, 34
Menon H., Wesolowski L., Zheng G., Jetley P., Kale L., Quinn T., Governato F., 2015, Comput. Astrophys. Cosmol., 2, 1
Merritt D., 1996, AJ, 111, 2462
Mesinger A., 2016, Understanding the Epoch of Cosmic Reionization Astrophysics and Space Science Library, Vol. 423. Springer International Publ., Switzerland
Misner C. W., Thorne K. S., Wheeler J. A., 1973, Gravitation. Princeton Univ. Press, Princeton
Mocz P., Lancaster L., Fialkov A., Becerra F., Chavanis P.-H., 2018, Phys. Rev. D, 97, 083519
Navarro J. F., Eke V. R., Frenk C. S., 1996a, MNRAS, 283, L72
Navarro J. F., Frenk C. S., White S. D. M., 1996b, ApJ, 462, 563
Nozières P., 1964, Theory of Interacting Fermi Systems. Frontiers in Physics, Benjamin
Peebles P. J. E., 1969, ApJ, 155, 393
Pillepich A. et al., 2018, MNRAS, 473, 4077
Runge E., Gross E. K. U., 1984, Phys. Rev. Lett., 52, 997
Ruth R. D., 1983, IEEE Trans. Nucl. Sci., NS-30, 2669
Sikivie P., Yang Q., 2009, Phys. Rev. Lett., 103, 111301
Sousbie T., Colombi S., 2016, J. Comput. Phys., 321, 644
Valluri M., Merritt D., 2000, Adv. Ser. Astrophy. Cosmol., 10, 229
Veltmaat J., Niemeyer J. C., Schwabe B., 2018, Phys. Rev. D, 98, 043509
Wigner E., 1932, Phys. Rev., 40, 749
Zhong L. et al., 2018, Phys. Rev. D, 97, 092001

APPENDIX A: METHOD OF CHARACTERISTICS AND LEAPFROG INTEGRATION

The Boltzmann-like system of axion infall in an Euclidean cosmology

$$0 = \partial_t f^{(1)} + \boldsymbol{v}\cdot\nabla f^{(1)} - \nabla\Phi'\cdot\nabla_v f^{(1)} - \nabla\bar{\Phi}\cdot\nabla_v f^{(1)} - m_a\nabla_v\cdot\left(\int \mathrm{d}^6 w_2 f^{(1)}(w_2,t)\nabla\Phi_{12} \times\left(\frac{C-1-(\lambda_1+\lambda_2)f_+}{1+\lambda_2 f_+}\right) f^{(1)}(w_2,t)\right), \quad \text{(A1)}$$

falls into the hyperbolic class of partial differential equations (PDEs). This class, which includes conservation laws and wave equations, is amenable to many elegant numerical solvers including the MOC. A Lagrangian method, the MOC propagates integrals of motion to a system of differential equations through parameter space, forming an accurate sample of the solution. For an extensive review of the technique, see Courant & Hilbert (1953). Conveniently, the Bose system equation of motion is of first order in derivatives, requiring only a less involved implementation of MOC. Time integration using the leapfrog integration method is also presented.

A1 Method of characteristics

A1.1 Theory

Using the notation of Courant & Hilbert (1953), the Boltzmann-like equation of motion of the correlated Bose fluid falls into the class of PDEs of the form

$$F(\{x_i\}, u, \{p_i\}) = 0 \quad \text{(A2)}$$

where $\{x_i\}$ are the n coordinates, u is the function to be solved for, dependent on the x_i, $\{p_i\}$ are fluxes given by partial derivatives $p_i = \partial_{x_i} u$, and the form of function F is first-order smooth in its arguments. F is seen to be an integral of motion. If u is any solution to the defining equation ($F = 0$), let us construct a curve in $\Re^{2n+1}$ of $(\{x_i(s)\}, u(s), \{p_i(s)\})$ such that $u(s) = u(x_i(s))$. Differentiating equation (A2) along the curve gives

$$\sum_i (\partial_{x_i} F + \partial_u F p_i)\dot{x}_i + \sum_i \partial_{p_i} F\,\dot{p}_i = 0. \quad \text{(A3)}$$

A constraint equation can also be found in u from the curve speed

$$\dot{u} - \sum_i p_i \dot{x}_i = 0 \quad \text{(A4)}$$

More generally, the implicitly differentiated form $\mathrm{d}u - \sum_i p_i \mathrm{d}x_i = 0$ also holds. A second constraint may be found from using the

exterior derivative language.

$$0 = d\left(du - \sum_i p_i dx_i\right)$$
$$= \sum_i \left(dp_i \dot{x}_i - \dot{p}_i dx_i\right). \tag{A5}$$

Altogether, these relations may be organized to provide equations of motion for the solution along the path

$$\dot{u} = \sum_i p_i F_{p_i}, \tag{A6}$$

$$\dot{x}_i = F_{p_i}, \tag{A7}$$

$$\dot{p}_i = -F_{x_i} - F_u p_i. \tag{A8}$$

A1.2 Application

For our application to the first-order axion Boltzmann-like equation, we map $u \to f$, $\{x_i\} \to (\boldsymbol{x}, \boldsymbol{v})$, $\{p_i\} \to (\nabla f, \nabla_v f)$, and F is the right-hand side of equation (A1). We see again that f is an integral of characteristic motion. Further, the equation form appears to be much like that from a Hamilton's principle with Hamiltonian F. We choose time to be the suitable parametrization of the characteristic. The characteristic equations are specifically found to be

$$\dot{f}_1 = 0 \tag{A9}$$

$$\dot{\boldsymbol{x}} = \boldsymbol{v} \tag{A10}$$

$$\dot{\boldsymbol{v}} = -\nabla\bar{\Phi} - m_a \frac{\partial}{\partial \nabla_v f_1} \int \mathrm{d}^6 w_2 \nabla\Phi_{12} \cdot \nabla_v \left(f_1 \frac{C - 1 - \lambda_+ f_+}{1 + \lambda_2 f_+} f_2\right), \tag{A11}$$

where the dot derivatives are now with respect to time, and $w_1 = (\boldsymbol{x}, \boldsymbol{v})$. For completeness, the functional derivative evaluates to

$$\frac{\partial}{\partial \nabla_v f_1} \int \mathrm{d}^6 w_2 \nabla\Phi_{12} \cdot \nabla_v \left(f_1 \frac{C - 1 - \lambda_+ f_+}{1 + \lambda_2 f_+} f_2\right)$$
$$= \int \mathrm{d}^6 w_2 \nabla\Phi_{12} \left(\frac{C - 1 - \lambda_+ f_+}{1 + \lambda_2 f_+} f_2\right)$$
$$+ \int \mathrm{d}^6 w_2 \nabla\Phi_{12} \left(f_1 \frac{-\lambda_+/2}{1 + \lambda_2 f_+} f_2\right)$$
$$- \int \mathrm{d}^6 w_2 \nabla\Phi_{12} \left(f_1 \frac{\lambda_2/2(C - 1 - \lambda_+ f_+)}{(1 + \lambda_2 f_+)^2} f_2\right). \tag{A12}$$

We can clearly see from this how the physics of individual sample points differs from the standard Newton's second law of classical CDM literature, sourced by the non-trivial correlation function. It is worth noting that the solution to these samples is exact to the order of accuracy of the Boltzmann equation, so long as the potentials and forces are known. The parabolic Poisson PDE for the gravitational potential must also be solved at each distribution sample, in order to calculate the gravitational force contribution. Techniques for solving the gravitational potential of an N-body sample often implement some artificial smoothing length to represent the contribution from a representative volume of phase space about a sample point; this is where exactness of modern gravitational MOC N-body implementations breaks down, though it is still for our purposes very useful.

In practice, MOC is used to track many sample characteristics from some initial Cauchy surface to a prescribed end time. As the DF is constant along these characteristic curves, choosing sample points according to distribution weight creates an effective distribution sampling from which equal-time observables may be calculated. These sample points are often referred to as particles or bodies, though they do not map directly to individual axions. Sampling of the DF often looks like an optimization between accurately reproducing the interactions and providing a clear means of interpreting the output configuration. In terms of the chosen gravitational sampling kernel of Section 5, the total force felt by an N-body particle amounts to

$$\boldsymbol{F}_1 = -\sum_i^n \nabla\Phi_{1i} - \sum_i^n \nabla\Phi_{1i} \left(\frac{C - 1 - \lambda_+(f_1 + f_i)/2}{1 + \lambda_2(f_1 + f_i)/2}\right)$$
$$- \sum_i^n \nabla\Phi_{1i} \left(\frac{-\lambda_+ f_1/2}{1 + \lambda_2(f_1 + f_i)/2}\right)$$
$$+ \sum_i^n \nabla\Phi_{1i} \left(f_1 \frac{\lambda_2/2(C - 1 - \lambda_+(f_1 + f_i)/2)}{(1 + \lambda_2(f_1 + f_i)/2)^2}\right), \tag{A13}$$

where Φ_{ij} is the intersample K1 Newtonian potential kernel.

A2 Leapfrog symplectic integration with exchange–correlation force

After the MOC, there is still one dimension left to partition before the axion fluid can be translated to a machine algorithm. Both the continuum and phase space discretized sample points derived above preserve the structure of phase space via $\dot{f} = 0$ and integral masses. We choose the leapfrog symplectic integrator to map the distribution over successive time-steps as it is designed to preserve volumes in phase space.

From the MOC derivations above, we can see that the particle equations of motion allow for a first-order operator equation interpretation

$$\dot{w} = \hat{O} w, \tag{A14}$$

where $w = (\boldsymbol{x}, \boldsymbol{v})$ and $\hat{O}$ is the system's evolution operator. The evolution operator of the sample can be written as

$$\hat{O} = \hat{T} + \hat{V}_{\bar{\Phi}} + \hat{V}_{XC}, \tag{A15}$$

where $\hat{T}$ is the standard non-relativistic kinetic operator, $\hat{V}_{\bar{\Phi}}$ is the mean field gravity operator, and $\hat{V}_{XC}$ is the XC operator. The leapfrog algorithm requires that the evolution operator is separable over its position and momentum dependence. Fortunately, each sample's DF value is invariant along characteristic curves, removing explicit velocity dependence in the XC force, at least of the order of accuracy of the integration scheme. It is therefore possible to separate the operator equation of motion into components exclusively dependent on the velocity or position sub-spaces of phase space. Leapfrog integration can therefore be implemented in the usual way. Applied to our axion system, the equations of motion for a sample particle become

$$\boldsymbol{x}(t/2) = \boldsymbol{x}(0) + \boldsymbol{v}(0)\frac{t}{2}, \tag{A16}$$

$$\boldsymbol{v}(t) = \boldsymbol{v}(0) - t\left(-\sum_i^n \nabla\Phi_{1i}^{K1} - \sum_i^n \nabla\Phi_{1i}^{K1} \times \left(\frac{C-1-\lambda_+(f_1+f_i)/2}{1+\lambda_2(f_1+f_i)/2}\right) - \sum_i^n \nabla\Phi_{1i}^{K1}\left(\frac{-\lambda_+ f_1/2}{1+\lambda_2(f_1+f_i)/2}\right) + \sum_i^n \nabla\Phi_{1i}^{K1}\left(f_- \frac{\lambda_2/2(C-1-\lambda_+(f_1+f_i)/2)}{(1+\lambda_2(f_1+f_i)/2)^2}\right)\right)\Bigg|_{\boldsymbol{x}(t/2)}, \tag{A17}$$

$$\boldsymbol{x}(t) = \boldsymbol{x}(t/2) + \frac{\boldsymbol{v}(t)}{m}\frac{t}{2}. \tag{A18}$$

where again the subscript '1' indicates evaluation at $(\boldsymbol{x}, \boldsymbol{v})$.

APPENDIX B: COMPLETED PLOTS AND RESULTS FROM MAIN DISCUSSION

Here, we present in more detail the results of Section 7. This includes the figures from the Top-hat simulations and several complementary figures. Further observations of unique Bose structure can be seen in Appendix C.

Following the central distribution of matter as it evolves through infall and virialization displays several elements of Unique Bose structure, Fig. B1. An increase in the rate of collapse to shell crossing is seen, up to ∼20 per cent among Gaussian initial conditions at $C = 0.5$ and ∼30 per cent faster infall for Top-hat. Faster collapse is first demonstrated in LQR and expanded on in Section 3. Chaotic dynamics and violent relaxation of the halo's most extreme phase characterize the evolution immediately following first shell crossing. We find violent relaxation damps after many local crossing times, or several system dynamical times, into a more settled quiescent phase of evolution by $T \sim 4t_{\rm dyn}$. The chaotic phase of Bose simulations passes more quickly, with the most correlated systems entering quiescent phase more than one dynamical time earlier than the classical systems. Halo spin seems to have only a weak effect on the features of collapse time, length of the chaotic phase, and resulting central mass.

The radial density profile, the standard global measure of halo structure, displays little sensitivity to XC. Radial density profiles of Gaussian infall show a universal broken power law suggestive of the cosmologically universal shape of NFW (Navarro et al. 1996a, b), Fig. B2. The haloes with static cosmological scale factor show a stee per central cusp of $\alpha \approx -1.7$, breaking slowly at $r_{\rm scale} \sim 0.4R$ into an outer power law of $\beta \sim -2.8$. Some small changes in the density profiles that scale with correlation are seen at and beyond the virial radius, around ∼2–3R. The virial radius is defined here to be the radius beyond which less than five crossing times have elapsed. The dependence of the breaking radius with spin is weak, much like in cosmological CDM. No significant new structure in the form of a central core or other features are seen for Bose Gaussian collapse. This insensitivity to correlation is surprising, as XC forces would be expected to be significant for highly correlated condensates. The scale radius of NFW is an emergent length in the otherwise scale-free system of CDM collapse. A similar phenomenon appears to occur with the Gaussian haloes. Further, the Gaussian halo's breaking scale is also insensitive across the full range of sampled correlations. Such robustness is unexpected. Further, as the underlying physics of the XC self-gravity contains no new scales, Bose haloes provide an independent measure of emergent scales among self-gravitating systems. However, Top-hat halo densities display some XC-induced effects, sub-dominant to the response to halo spin, especially at the highest tested spin. We find Top-hat density profiles are characterized by an outer power law of power $\beta \sim -4.0$ breaking into milder behaviour centred around $\alpha \approx -1.0$ among spinning haloes and $\alpha \approx -2.0$ for spin-less ones. The breaking scales are primarily dependent on spin.

In general, a halo's high-resolution phase-space density profile is expected to contain a superposition of falling and rising radial cold sheets of fluid and their turn-around caustics. Though only the first and perhaps second caustics can be resolved at the outermost radii

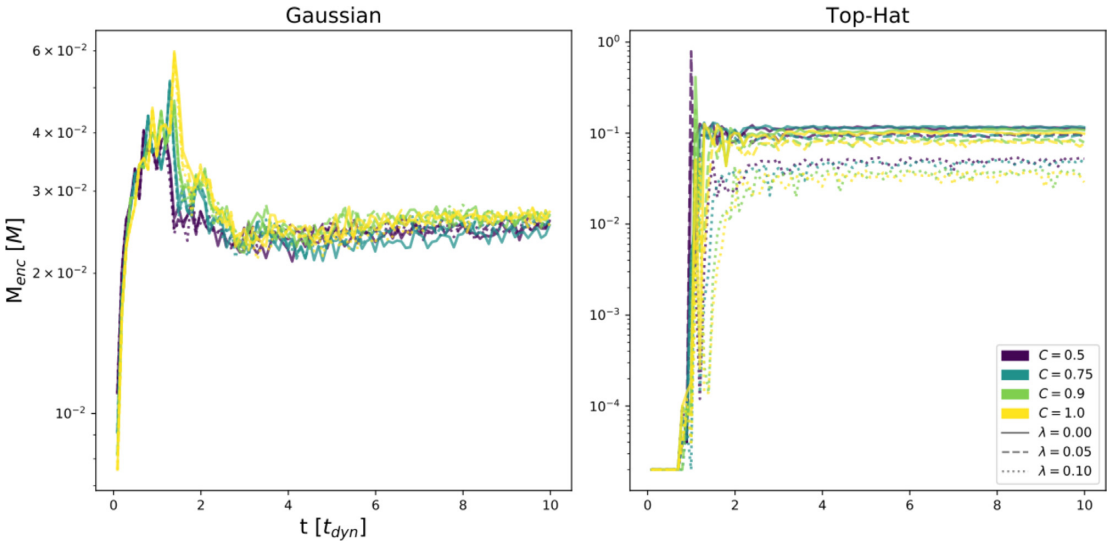

Figure B1. Mass within central $r = 0.05R$ of halo over time of all isolated collapse simulations of Section 6. (Left) Gaussian profiles, (Right) Top-hat profiles. Profile coloration indicates degree of correlation ranging from classical $C = 1.0$ to highly correlated $C = 0.5$. Line style indicates level of Peeble's spin λ of the halo. The time to collapse is seen to be shorter for correlated haloes, as is the time between first infall and virialization. Note that the vertical scale is different for each plot.

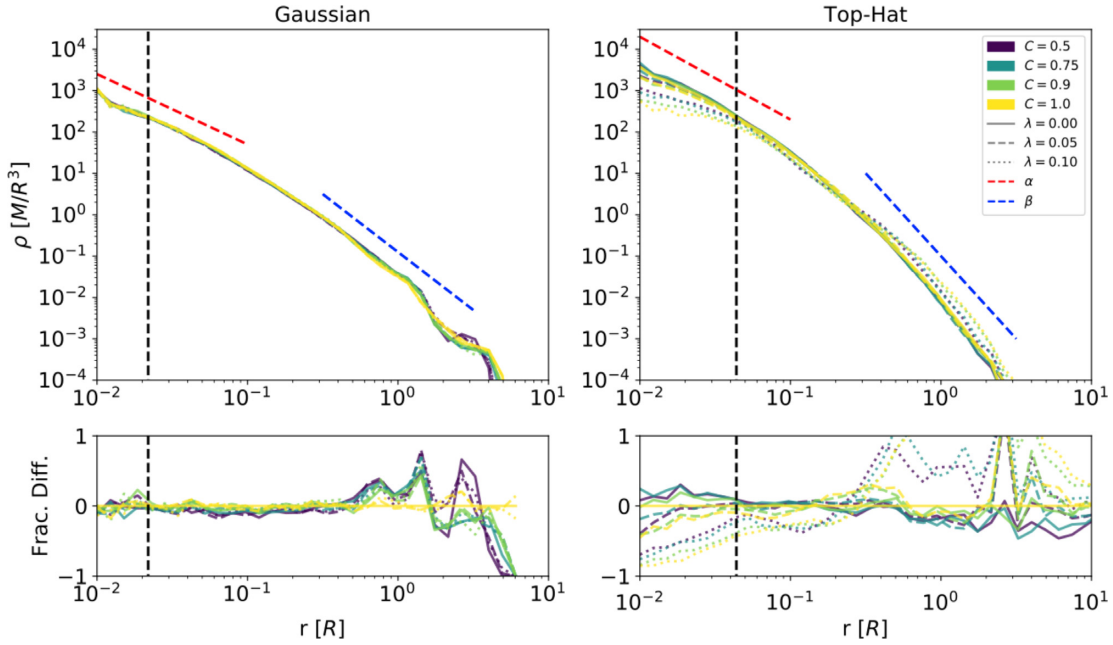

Figure B2. Mass density radial profiles of the isolated collapse simulations of Section 6 after $10t_{\rm dyn}$. (Left) Gaussian profiles, (Right) Top-hat profiles. (Top) Raw measurements, (Bottom) fractional differences from the classical spin-less halo. Profile coloration indicates degree of correlation ranging from classical $C = 1.0$ to highly correlated $C = 0.5$. Line style indicates level of Peeble's spin λ of the halo. Comparison power laws are given for the inner (α) and outer (β) halo structure. The softening profile's maximum force radius is represented by the black dashed line in each simulation set, below which our confidence in the results is diminished.

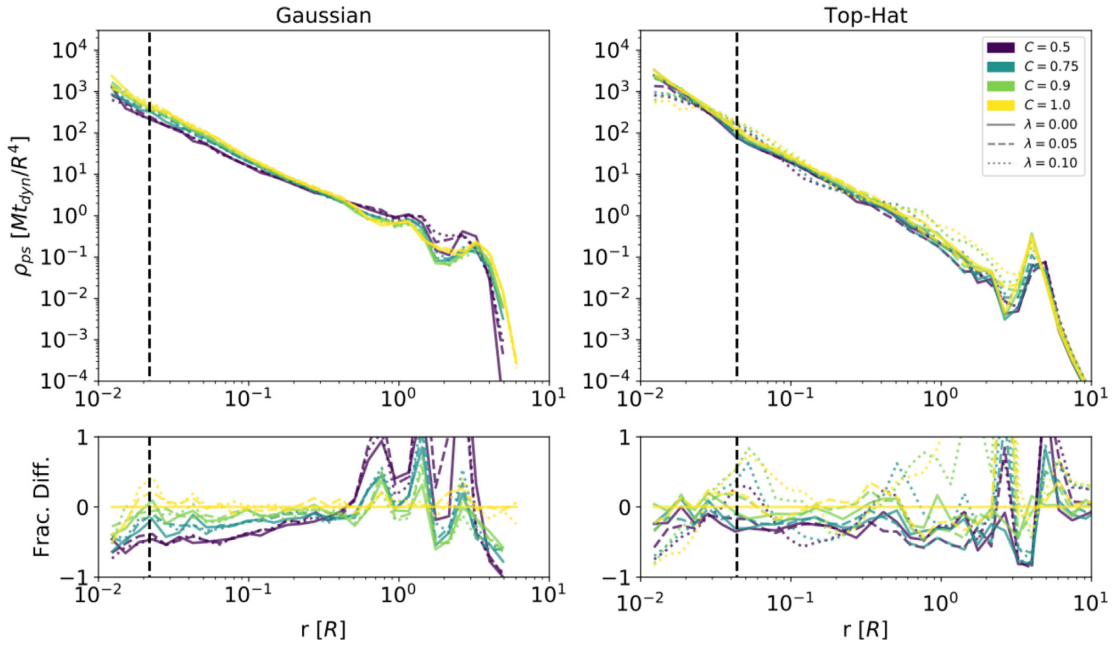

Figure B3. Phase space mass density radial profiles of the isolated collapse simulations of Section 6. (Left) Gaussian profiles, (Right) Top-hat profiles. (Top) Raw measurements and (Bottom) fractional differences from the classical spin-less halo. Haloes were measured after evolving for $10t_{\rm dyn}$. Profile coloration indicates degree of correlation ranging from classical $C = 1.0$ to highly correlated $C = 0.5$. Line style indicates level of Peeble's spin λ of the halo. Volume in velocity space is measured in the local spherical velocity dispersion. The softening profile's maximum force radius is shown by the black dashed line in each simulation set, below which our confidence in the results is diminished.

of these modestly resolved haloes, more substantial changes can be seen in the mean phase space density, Fig. B3. Gaussian phase space densities show well-consolidated correlation-dependent shifts, with virtually all of the spread at inner radii being attributed to the large differences in velocity dispersion, Fig. B4, which shows significant effects induced by XC interactions. Note that in the figure, where the profiles of Bose and uncorrelated haloes intersect in density and velocity dispersion, is the same as the density profile scale radius. Top-hat haloes show differences that depend on correlation for large radii and on spin for small radii. The increased

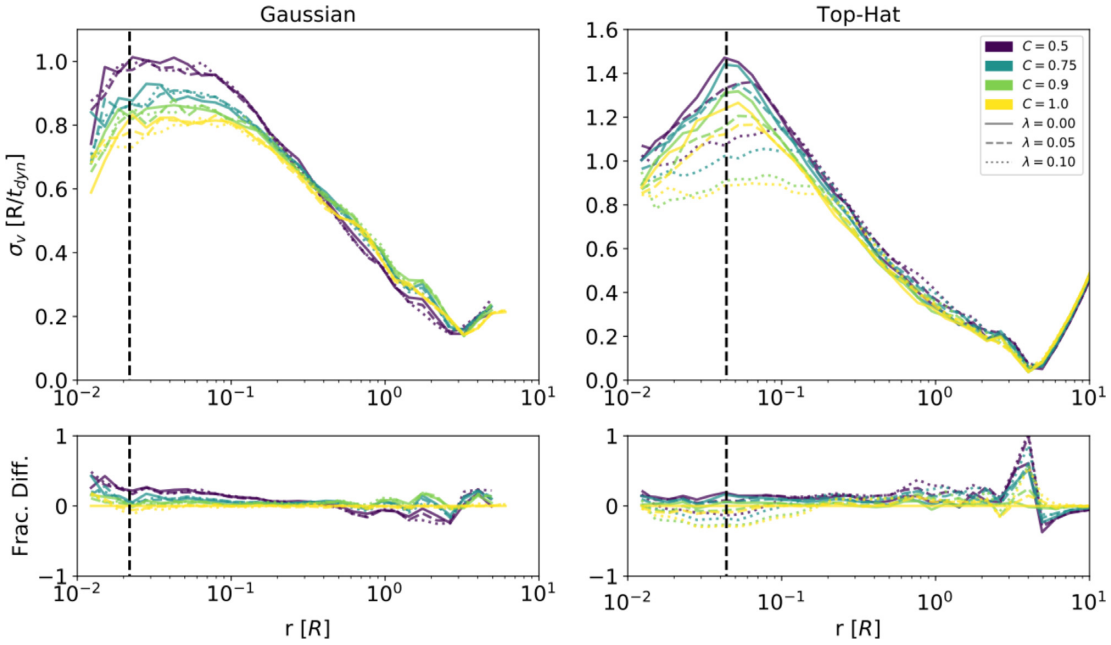

Figure B4. Spherical velocity dispersion radial profiles of the isolated collapse simulations of Section 6 after $10t_{\rm dyn}$. (Left) Gaussian profiles and (Right) Top-hat profiles. (Top) Raw measurements and (Bottom) fractional differences from the classical spin-less halo. Profile coloration indicates degree of correlation ranging from classical $C = 1.0$ to highly correlated $C = 0.5$. Line style indicates level of Peeble's spin λ of the halo. The softening profile's maximum force radius is shown by the black dashed line in each simulation set, below which our confidence in the results is diminished.

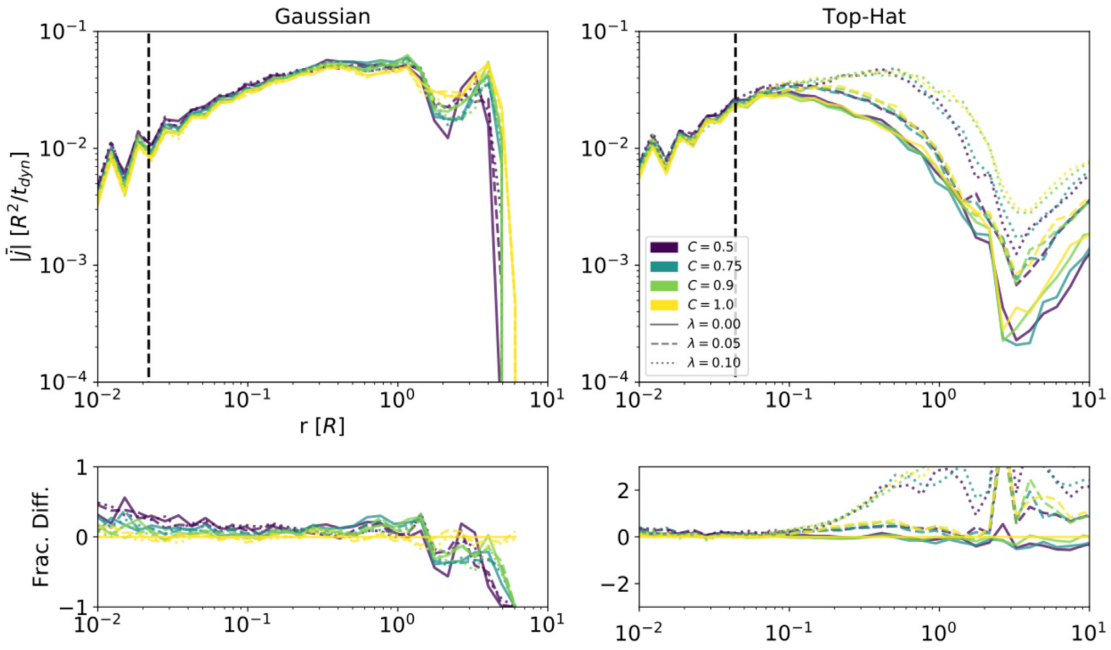

Figure B5. Mean magnitude angular momentum radial profiles of the isolated collapse simulations of Section 6. (Left) Gaussian profiles, (Right) Top-hat profiles. (Top) Raw measurements, (Bottom) fractional differences from the classical spin-less halo. Haloes were measured after evolving for $10t_{\rm dyn}$. Profile coloration indicates degree of correlation ranging from classical $C = 1.0$ to highly correlated $C = 0.5$. Line style indicates level of Peeble's spin λ of the halo. The softening profile's maximum force radius is shown by the black dashed line in each simulation set, below which our confidence in the results is diminished.

velocity dispersion also also increases the classical virialization ratio.

Radial profiles of angular momentum and velocity dispersion show stronger effects than for density, Figs B4 and B5. Gaussian haloes, as mentioned above, show clear augmentation of velocity dispersion with correlation, with transitions from amplification to compression occurring at the breaking radius. Velocity dispersion is fairly insensitive to spin. Top-hat haloes also show clear amplification of dispersion, but no transition into compression. Shapes of the Top-hat velocity dispersion profiles change notably with spin. Spin-less haloes show a low-radius dispersion peak near the softening length. Spun haloes flatten this peak and shift their maxima to higher radii, where the dispersions of the spun haloes converge with the spin-less haloes. Sample angular momentum differences

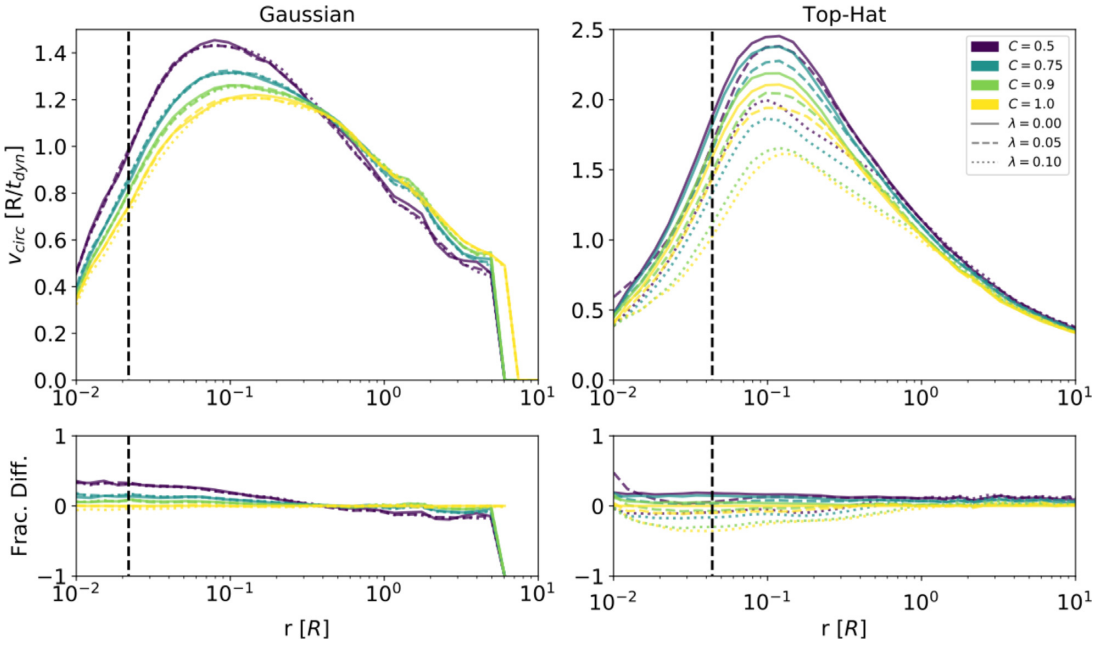

Figure B6. Circular orbit speed radial profiles of the isolated collapse simulations of Section 6 after $10t_{\rm dyn}$. (Left) Gaussian profiles and (Right) Top-hat profiles. (Top) Raw measurements and (Bottom) fractional differences from the classical spin-less halo. Profile coloration indicates degree of correlation ranging from classical $C = 1.0$ to highly correlated $C = 0.5$. Line style indicates level of Peeble's spin λ of the halo. The softening profile's maximum force radius is shown by the black dashed line in each simulation set, below which our confidence in the results is diminished.

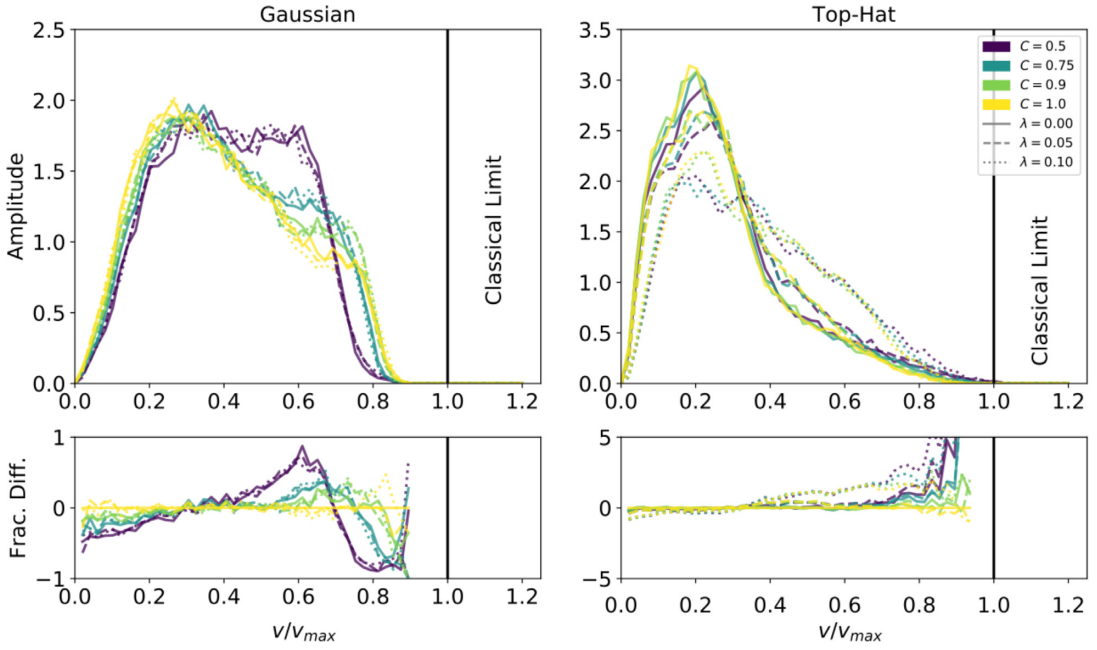

Figure B7. DFs of speed fraction over classical gravitational potential $v/v_{\rm max} = v/\sqrt{2|\tilde{\Phi}|}$ of isolated collapse simulations of Section 6. (Left) Gaussian profiles and (Right) Top-hat profiles. (Top) Raw measurements and (Bottom) fractional differences from the classical spin-less halo. Haloes were measured after evolving for $10t_{\rm dyn}$. Distributions are taken from within $r = 0.4R$ for Gaussian simulations and $r = 1.0R$ for Top-hat. Profile coloration indicates degree of correlation ranging from classical $C = 1.0$ to highly correlated $C = 0.5$. Line style indicates level of Peeble's spin λ of the halo. Sample points lying outside of the classical limit occur only with haloes of correlation $C = 0.75$ or stronger, and amount to about one tenth of a per cent of the sampled mass. Note that the vertical scale is different for each plot.

with respect to correlation are less pronounced, possibly due to the relatively conserved status of angular momentum in a system with spontaneously broken rotational symmetry. Most particle angular momentum evolution is induced by the radial orbit instability (ROI) symmetry-breaking feature. Correlations consistently produce a first higher, and then lower mean angular momentum as the radius increases for Gaussian haloes, with the curves again intersecting at the breaking radius. Top-hat collapses behave similarly at small radii, eventually separation according to spin. Each spin exhibits its own structure.

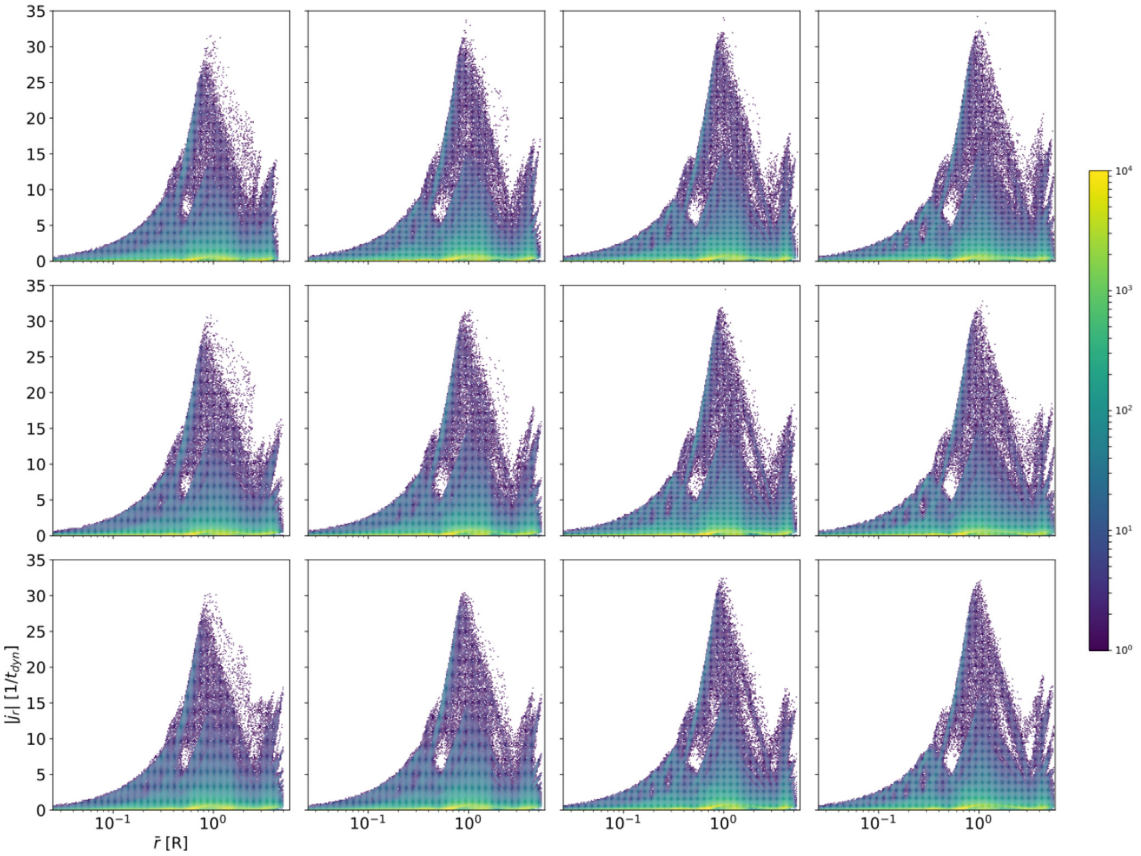

Figure B8. Radial orbital action and mean orbit radius distributions of Gaussian isolated collapse simulations. Panels are organized by correlation (column wise: $C = 0.5, 0.75, 0.9, 1.0$ left to right) and spin (row wise: $\lambda = 0.0, 0.05, 0.1$ top to bottom). Samples are taken from 100 equally spaced frames during 10–12$t_{\rm dyn}$. Sample points are taken such that each particle is given a single mean radius and the radial autocorrelation power spectrum.

Circular-orbit speed profiles are a proxy for experienced force-per-particle, and quantify much of the virialized halo dynamics (Fig. B6). Each profile follows an expected curve as the density steepens with rapidly increasing enclosed mass, before levelling out and dropping at large radii where new mass is absent. The differences in force between the correlated curves are large. The most highly correlated $C = 0.5$ experience up to a 70 per cent higher-than-classical at peak force, more than twice classical at the centre, and lower than classical force in the outer reaches in the Gaussian haloes. The force augmentation translates into differences in the circular speed curves of up to 45 per cent at any given radius, and a 20 per cent increase in maximum speed. Bose Top-hat haloes also have an increase in force of up to 70 per cent and an increase of rotational speed by over 30 per cent. Again, it is surprising that higher acceleration of sample points does not much change the spatial structure of the halo. The crossing between stronger-than-classical and weaker-than-classical force occurs near the breaking radius among Gaussian haloes, coinciding with similar transitions in the velocity dispersion and classical energy. Bose Top-hat haloes have higher-than-classical force throughout.

Classical haloes, evolving well into quasi-equilibrium, obey a simple classical energy constraint: bodies with kinetic energy above the asymptotic potential binding are unbounded and will separate themselves from the system of the order of the crossing time. As our haloes are several crossing times into their virialized states, there should be few unbounded bodies remaining in the classical haloes. Bose fluids do not necessarily obey this condition as they are subject to an additional interaction not captured in the gravitational potential. Regular violation of the classical energy condition is another possible marker of unique Bose structure.

Bose haloes show a definite shift of their velocity distribution with respect to the classical binding limit $v_{\rm max} = \sqrt{2\tilde{\Phi}}$, Fig. B7. Angular momenta, speeds, and other kinetic quantities have their own form of the classical energy constraint. Speed is shown here, since it is expected to produce a larger effect than, say, angular momentum, which is subject to equipartition of velocity in-so-far as a virialized structure allows. Sampling of haloes is taken on the sub-set of the halo where the fractional and overall XC forces are highest, within the scale radius $r_G = r_{\rm scale} = 0.4R$ for Gaussian haloes and Top-hat haloes inside of $r_{\rm TH} = 1.0R$. Classical structures obey the binding energy limit in both sets of collapses. The classical shape among Gaussian haloes is a single low-speed peak at $v/v_{\rm max} \approx 0.25$, with a smooth tail that turns steeply at $v/v_{\rm max} \approx 0.8$. Gaussian Bose haloes have slower tails at both the high-speed and low-speed ends, with the high-speed tail extending slightly beyond the classical cut-off, and with the bulk of the distribution shifting slowly to the double-lobed plateau seen in $C = 0.5$ haloes. Distribution centres of mass are weakly dependent on correlation, staying close to $\langle v/v_{\rm max}\rangle \approx 0.4$. Top-hat haloes are closer to a thermal distribution in shape, with long high-speed tails. Each spin group has its own class of shapes. Distributions within each spin change with correlation, becoming depleted at low speed and elongating the high-speed tail beyond the the classical limit. Double peaks are also observed for Top-hat haloes of high spin and correlation.

The binding-condition-violating sub-population among Top-hat simulations is a small but predictable group from our studies. Spin of the halo does not play a significant role in the size of this sub-population. Condition-violating samples are present throughout the halo volume, save for the edge of the outermost orbiting phase-space sheets. The lack of binding-condition-violating bodies in Gaussian haloes is perhaps due to the generally softer infall of the normal profile, resulting in less work done on individual particles. This implies there are no unbound bodies at any value of correlation among Guassian haloes.

Measuring speed distribution changes in the DM of an isolated halo is difficult to accomplish by measuring baryons. Stellar populations are not directly subject to the Bose modified gravity from XC, only the total Newtonian gravitational potential. Axion searches sensitive to a halo's local energy distribution may be capable of resolving differences in the kinetic makeup of a Bose halo. Another means to observe the explicit DM motion may come from the velocities and organization of satellite galaxies and other halo sub-structures.

The moderate resolution of a single time-slice in a simulation prevents more from being easily said regarding the nature of halo structure. The next sub-section introduces a method of stacking time slices in order to explore the orbital motions and improve resolution of measurements.

The particle distribution in a self-gravitating virialized halo is known to be non-thermal, producing resonances and other structures as a byproduct. Halo forces point primarily in the radial direction, and these strong forces are capable of setting the radial action into particular modes of motion. These resonances may appear as local fine structure in a halo's energy distribution or other features such as a turn-around caustic. Fine phase space structures are visible at all radii in all simulations, Fig. B8. New structure is visible in these fine branching features. For example, counting in from the most prominent branch in Fig. B8, which peaks at $\bar{r} \sim 1R$, one sees 10–12 distinct branches in CDM haloes down to the radius $\bar{r} = 0.04R$. Noise, and force softening subdues structures much below $\bar{r} = 0.04R$. The number of branch structures increases with correlation, reaching 18 for $C = 0.5$, becoming crowded to the point of large overlaps in mean radius. The more crowded Bose spectra also look more self-similar in shape than their CDM counterparts. The inner orbital structures are unfortunately at the resolution limit at the current levels of softening and time resolution, though a number of other coherent features can be seen at larger radii beyond the virial radius. More resolved Bose fine structure requires improved simulations.

APPENDIX C: FURTHER MARKERS OF BOSE STRUCTURES

Several more signatures of Bose physics were uncovered during the study of the virialized haloes, including

(i) Shifts in the classical binding energy radial profile of the order of $\gtrsim 400(1 - C)^2$ per cent.
(ii) New sub-structures in classical energy and angular momentum distributions.
(iii) Small sub-populations of halo particles violating the classical binding condition of virialized systems.
(iv) Compactification of orbital actions in all three independent dimensions.
(v) Evidence of correlation-induced mixing across the virial radius.
(vi) Notable *lack* of effects on the halo density and anisotropy profiles.

This appendix covers these results, which have been organized according to their extent, and a short discussion of those results.

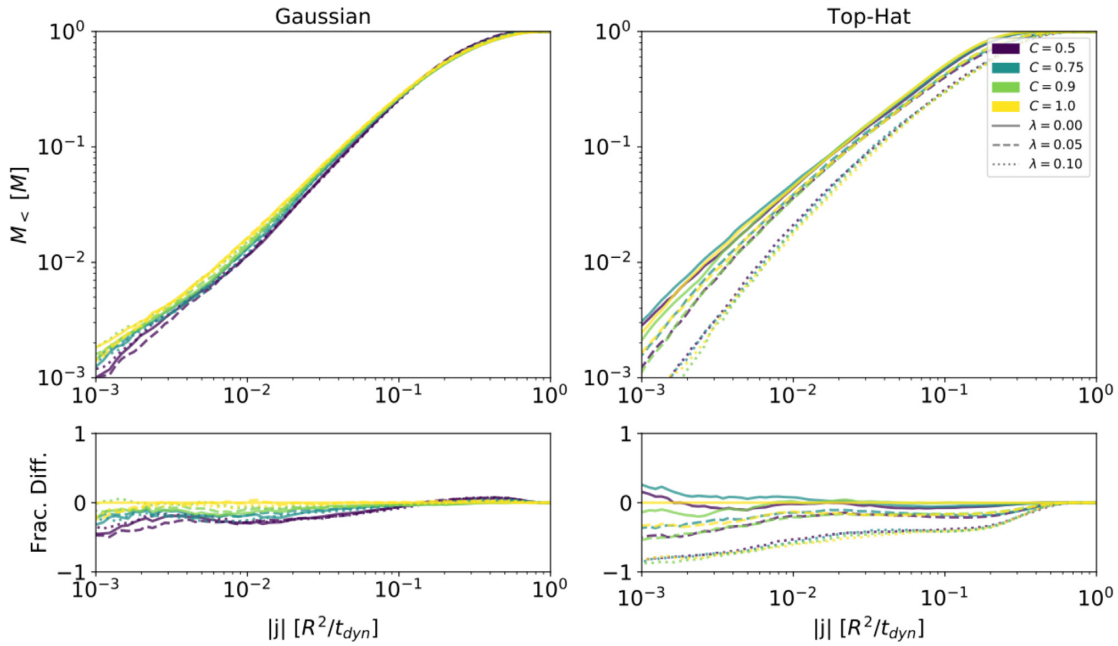

Figure C1. Enclosed mass angular momentum profiles of the isolated collapse simulations of Section 6 after $10t_{\rm dyn}$. (Left) Gaussian profiles, (Right) Top-hat profiles. (Top) Raw measurements, (Bottom) fractional differences from the classical spin-less halo. Profile coloration indicates degree of correlation ranging from classical $C = 1.0$ to highly correlated $C = 0.5$. Line style indicates level of Peeble's spin λ of the halo. The lower limit in mass is given by 50 sample points.

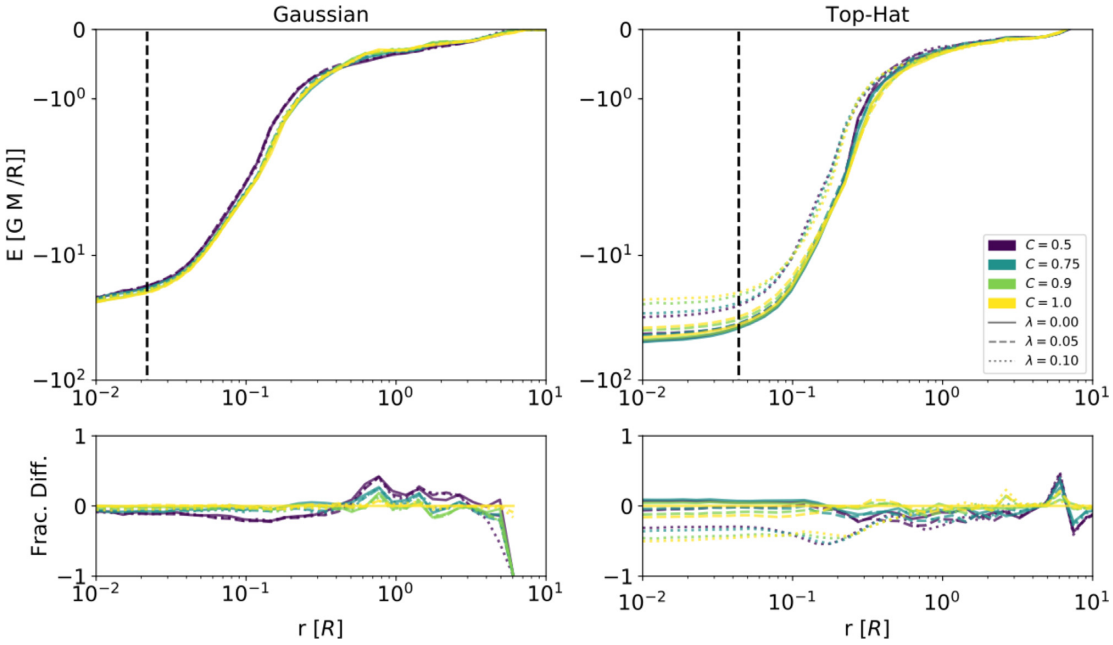

Figure C2. Classical binding energy radial profiles of the isolated collapse simulations of Section 6. (Left) Gaussian profiles, (Right) Top-hat profiles. (Top) Raw measurements, (Bottom) fractional differences from the classical spin-less halo. Haloes were measured after evolving for $10t_{\rm dyn}$. Profile coloration indicates degree of correlation ranging from classical $C = 1.0$ to highly correlated $C = 0.5$. Line style indicates level of Peeble's spin λ of the halo. The softening profile's maximum force radius is shown by the black dashed line in each simulation set, below which our confidence in the results is diminished.

C1 Global features

Another standard measure of classical infall after the radial density profile is provided by the enclosed mass as a function of angular momentum $M_<(j)$ (Bullock et al. 2001), Fig. C1, and shows weak but increasing differences with correlation. Gaussian profiles show a relative depletion of mass over the first decades of observed angular momentum, with little sensitivity to spin. The Gaussian simulations classically maintain a universal concave upwards shape, characterized by a breaking angular momentum roughly at $j_{\rm scale} \approx 10^{-2}R^2/t_{\rm dyn}$ between two power laws, as opposed to the single power law of cosmological haloes found by Bullock et al. (2001). The profiles shown are ordered by correlation and become insensitive to spin over the high angular momentum region, but begin to diverge at lower angular momentum. More highly correlated haloes are also seen to reach total mass at lower angular momenta than the classical haloes. The Top-hat simulations show different profiles, primarily separated by spin, but with additional stratification with XC. The shape of Top-hat profiles vary with spin. Spin-less haloes are dominated by a single power law of $\alpha \approx -1.25$. Rotating haloes are relatively depleted of low angular momentum material and demonstrate downwards concavity throughout.

Classical binding energy per-particle is another near integral of motion of the classical virialized halo (Fig. C2). Classical energy density is an integral of the motion when quasi-equilibrium is satisfied, and then only for classical samples with an effective Hamiltonian with canonical kinetic and potential terms. Bose halo fluid elements are not expected to have the integral of motion energy, though the system's total energy can be shown to be integral. The energy-per-particle radial profile does not have much spin dependence, but it is dependent on correlation. Bose haloes show a difference in per-particle energy over classical haloes of up to 25 per cent between $r = 0.1$–$0.2R$. Correlated haloes show deeper binding energy at these large radii. Bose Gaussian haloes are also smoother in profile. The more consistent and weaker dependence of energy among Bose haloes at large radii leads to a transition to shallower energies within the breaking radius. Top-hat halo energy profiles are also seen to be ordered by, and, for spin, can show a much higher separation in energy than Gaussian profiles. This is a result of the effect of spin to reduce the density at low radii, resulting in a shallower potential well than for classical haloes.

There exist instabilities for any simulations of cold near-spherical distributions occurring in three spatial dimensions. The well-studied ROI (Barnes, Hut & Goodman 1986; Valluri & Merritt 2000; Bellovary et al. 2008; Lentz, Quinn & Rosenberg 2016) is known to produce a prolate bar feature at the halo centre. Bose physics may leave a signature in this bar, in either the Top-hat or Gaussian haloes. The shape of the halo beyond the gross spherical or cylindrical symmetry is important to understand the tangential dynamical mechanisms, Fig. C3. Among Gaussian haloes, triaxalities generally range from moderately oblate to spherical-like at inner radii, increasing in prolate-ness until slightly outside the softening length $r \sim 0.05R$ and then relaxing to a modest prolate state for the remainder of the virialized volume. Bose haloes show a slightly greater tendency for prolate shape than classical haloes at large radii. While there are other differences in shape observed between the classical and Bose haloes, their behaviour with respect to amount of correlation and spin is not completely clear. Top-hat triaxalities show a steady trend among spin-less haloes from a spherical shape at inner radii to a more prolate shape of $T = 0.7$–0.8 farther out. Spun haloes are far more varied, with oblate or spherical shape at inner radii, just as for the Gaussian haloes, rising to near total prolate-ness before falling to a spherical or oblate shape at large radii. Again the role of correlation for these haloes is unclear.

The velocity anisotropy profile is nearly as robust to XC interactions as the mass density profile, Fig. C4. Weakly spun haloes generally show a velocity anisotropy in favour of motion in the radial direction as a consequence of their initial near-radial infall,

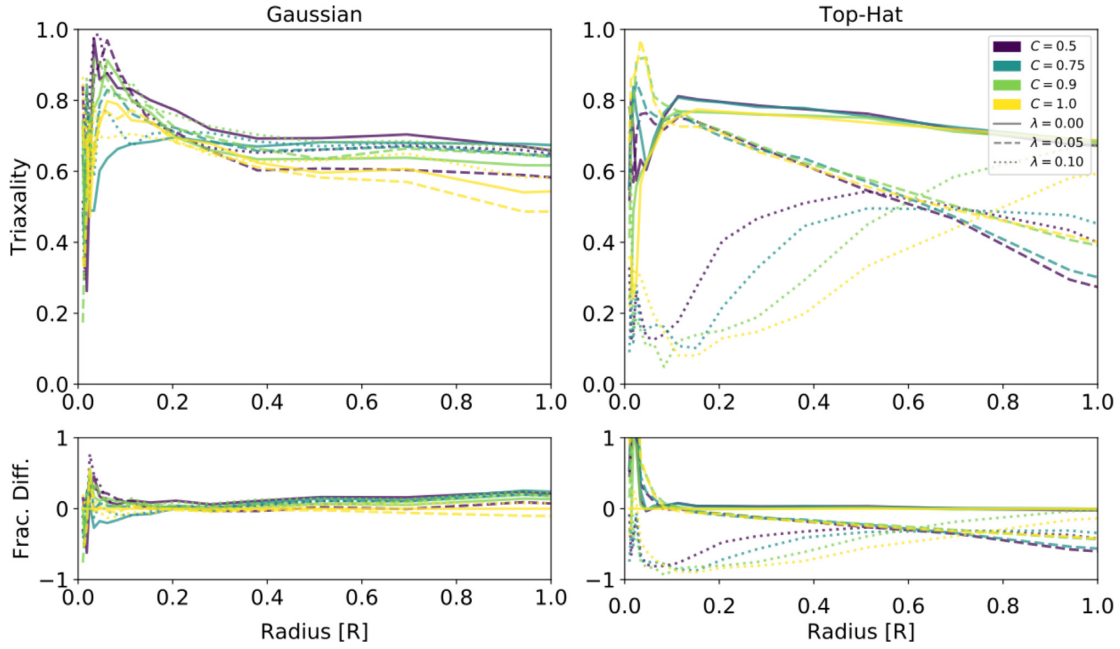

Figure C3. Triaxality radial profiles of the isolated collapse simulations of Section 6. (Left) Gaussian profiles and (Right) Top-hat profiles. (Top) Raw measurements and (Bottom) fractional differences from the classical spin-less halo. Haloes were measured after evolving for $10t_{\rm dyn}$. Profile coloration indicates degree of correlation ranging from classical $C = 1.0$ to highly correlated $C = 0.5$. Line style indicates level of Peeble's spin λ of the halo. The softening profile's maximum force radius is shown by the black dashed line in each simulation set, below which our confidence in the results are diminished.

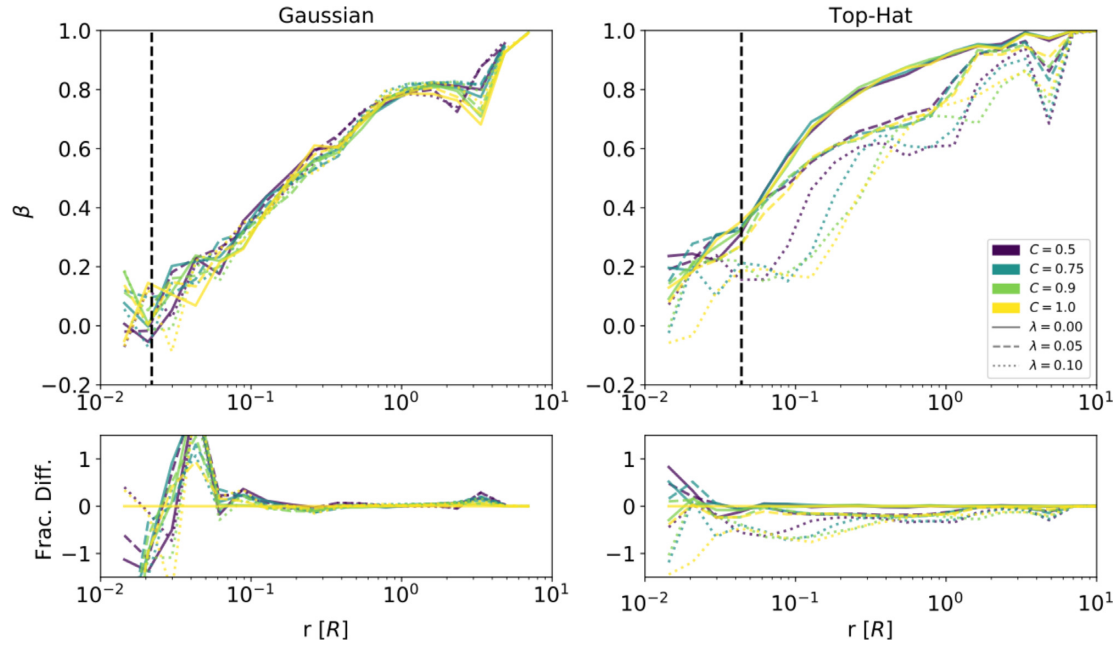

Figure C4. Velocity anisotropy radial profiles of the isolated collapse simulations of Section 6. (Left) Gaussian profiles, (Right) Top-hat profiles. (Top) Raw measurements, (Bottom) fractional differences from the classical spin-less halo. Haloes were measured after evolving for $10t_{\rm dyn}$. Profile coloration indicates degree of correlation ranging from classical $C = 1.0$ to highly correlated $C = 0.5$. Line style indicates level of Peeble's spin λ of the halo. The softening profile's maximum force radius is shown by the black dashed line in each simulation set, below which our confidence in the results is diminished.

though the collection of orbits tend towards velocity isotropy ($\beta \rightarrow 0$) at inner radii. Much of the virial volume among Gaussian haloes shows little discernible Bose structure. Only at the outer edge of the virial volume do haloes show features that depend on correlation, with more correlated haloes softening the hard break in anisotropy as one crosses the virial radius. A small shift in the radius of the virial break is also observed for the most highly correlated spinning haloes. All Top-hat haloes do not reach complete velocity isotropy. Each spin curve has its own profile shape. Correlation dependence is difficult to distinguish among the lower spin curves,

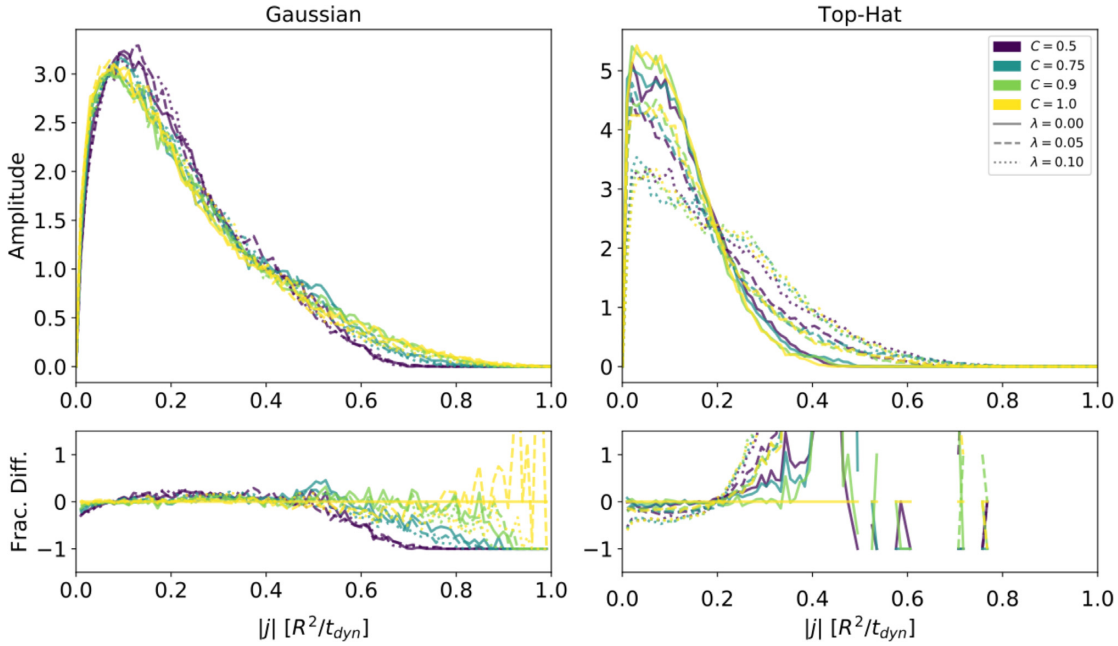

Figure C5. Magnitude angular momentum DF of the isolated collapse simulations of Section 6 after $10t_{\rm dyn}$. (Left) Gaussian profiles and (Right) Top-hat profiles. (Top) Raw measurements and (Bottom) fractional differences from the classical spin-less halo. Profile coloration indicates degree of correlation ranging from classical $C = 1.0$ to highly correlated $C = 0.5$. Line style indicates level of Peeble's spin λ of the halo. The plots are a rephrasing of the data presented in Fig. C1, with the emphasis placed on the local distribution.

though some coherent shifts are seen between the most highly spun haloes.

C2 Global distributions and dynamical law-breaking features

More direct projections of the final phase-space distribution reveal other novel Bose structures. Magnitude angular momentum among Gaussian simulations shows organization with correlation for their entire angular momentum domain, ending with an angular momentum cut-off depending only on correlation (Fig. C5). The angular momentum cut-off arises at lower angular momentum with increasing correlation, and may be an indication of the XC interaction suppressing the evolution of angular momentum. Top-hat halo curves expectantly divide first along spin, but secondly also show some correlation organization, most notably at $\lambda = 0.10$.

Classical binding energy distributions are also well organized, showing obvious changes in sub-structure (Fig. C6). Gaussian haloes, all with approximately the same minimum potential, show uniform growth for the most tightly bound objects, according to, for example, the radial density profile. The distributions at higher energy begin to diverge in shape according to correlation. Classical haloes are seen to have several highly populated regions above $E = -3GM/R$, with a central peak at $E \approx -GM/R$. The highest energy of these peaks and the adjacent low-energy trough become depleted with increasing XC forces through $C = 0.75$, after which the peak begins to shift to lower energies and somewhat re-establishes itself among $C = 0.5$ haloes. Correlated distributions also shift their lower energy distribution into a central consolidated feature, still centred at $E = -GM/R$. Top-hat energy structure is dominated by spin, but also displays obvious effects of correlation. Much of the observable correlated structure is in the form of more prominent high-energy bands, less prominent middle energy structures, and lower potential minima. Classically unbounded objects are not displayed in these distributions.

Classical haloes, evolving well into quasi-equilibrium, obey a simple classical energy constraint: bodies with kinetic energy above the asymptotic potential binding are unbounded and will separate themselves from the system of the order of the crossing time. As our haloes are several crossing times into their virialized states, there should be few unbounded bodies remaining in the classical haloes. Bose fluids do not necessarily obey this condition as they are subject to an additional interaction not captured in the gravitational potential. Regular violation of the classical energy condition is another possible marker of unique Bose structure.

The moderate resolution of a single time-slice in a simulation prevents more from being easily said regarding the nature of halo structure. The next sub-section introduces a method of stacking time slices in order to explore the orbital motions and improve resolution of measurements.

C3 Fine structure and orbital actions

Each halo is well settled into quasi-equilibrium after 10 dynamical times. A sub-sampling of single time-slice halo configurations, or 'snapshots', after virialization and prior to relaxation can be organized into a 'stack' of phase-mixed quasi-independent snapshots of the halo. The elements of such a stack can be co-added, effectively increasing the number of samples in the simulations. Extending several of the S simulations by another multiple dynamical times past the initial period of 10 dynamical times can also provide samples of particle orbits within the virial radius, allowing for an orbital analysis of the haloes. Stacking and orbit integration together create the most resolved observables of this analysis. The simulations chosen for extension are of Gaussian shape, with all sampled spins, with correlations $\{0.5, 0.75, 0.9, 1.0\}$, and are prolonged by two dynamics times.

True integral actions in a triaxial problem are difficult to construct, despite the limited number of actions needed to span a

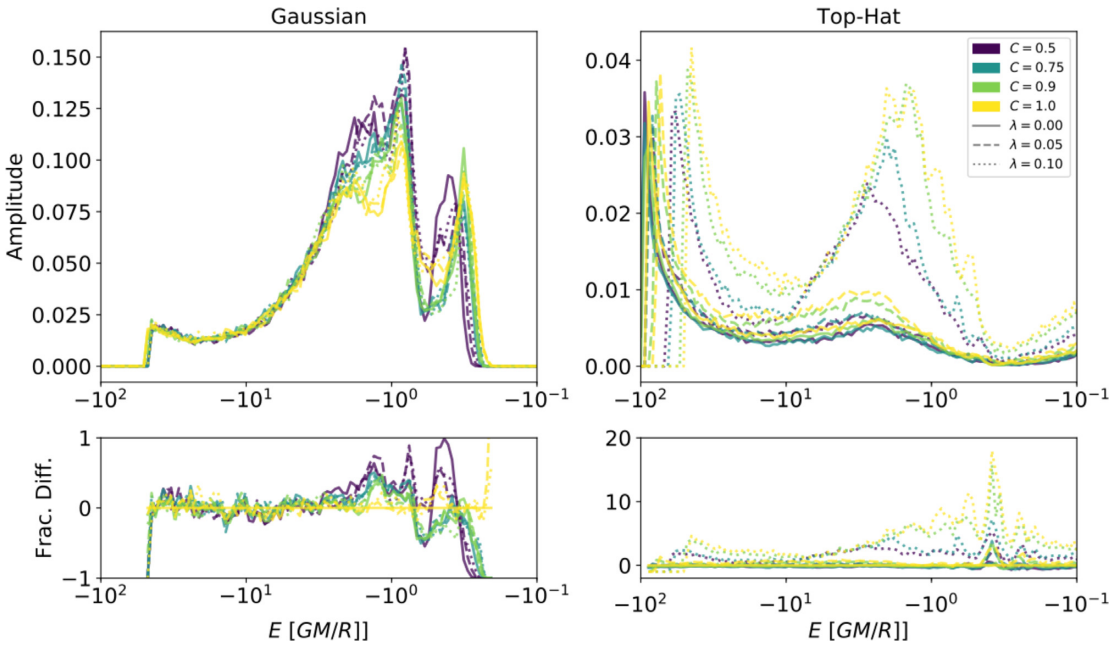

Figure C6. Classical binding energy DF of the isolated collapse simulations of Section 6. (Left) Gaussian profiles and (Right) Top-hat profiles. (Top) Raw measurements and (Bottom) fractional differences from the classical spin-less halo. Haloes were measured after evolving for $10t_{\rm dyn}$. Profile coloration indicates degree of correlation ranging from classical $C = 1.0$ to highly correlated $C = 0.5$. Line style indicates level of Peeble's spin λ of the halo. The energy is restricted to classically bound states.

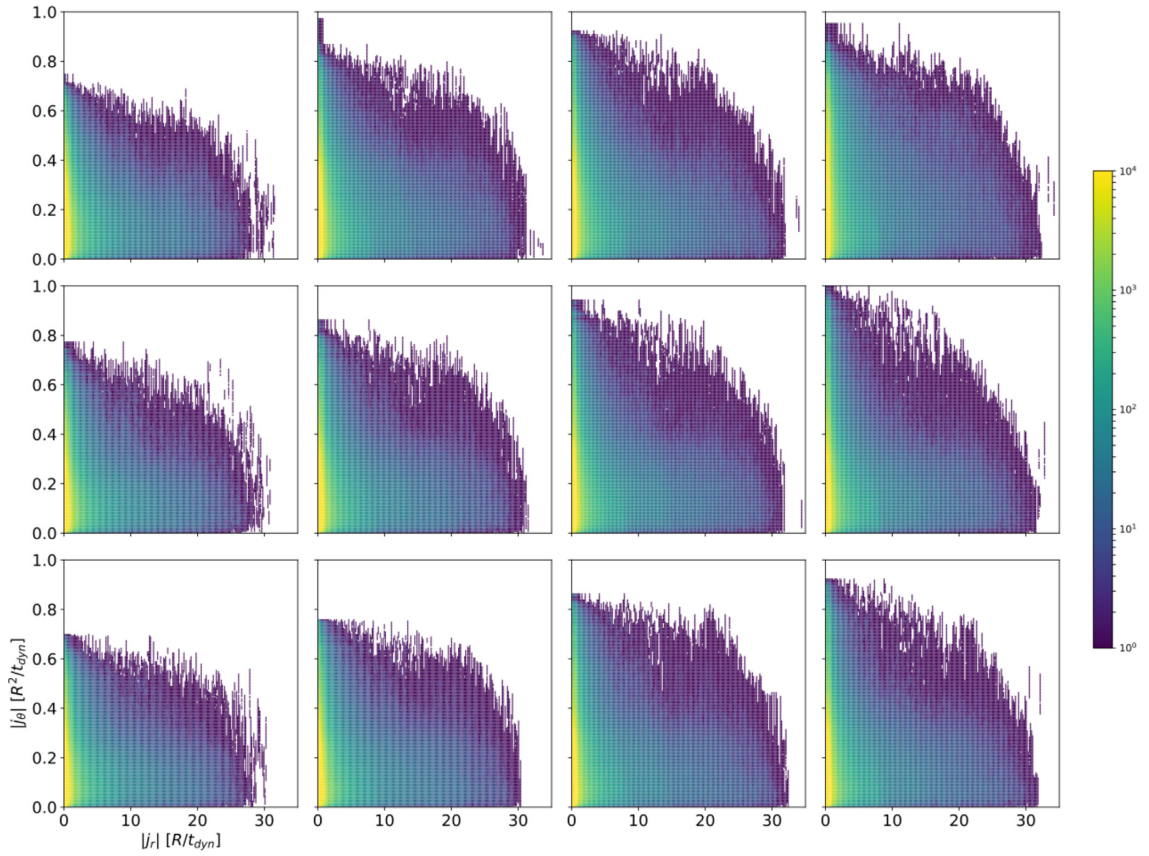

Figure C7. Radial and polar orbital action distributions of Gaussian isolated collapse simulations. Panels are organized by correlation (column wise: $C = 0.5$, 0.75, 0.9, 1.0 left to right) and spin (row wise: $\lambda = 0.0$, 0.05, 0.1 top to bottom). Samples are taken from 100 equally spaced frames during 10–$12t_{\rm dyn}$. Sample points are taken such that a particle's weights are given by the outer product of j_θ and the radial autocorrelation power spectrum.

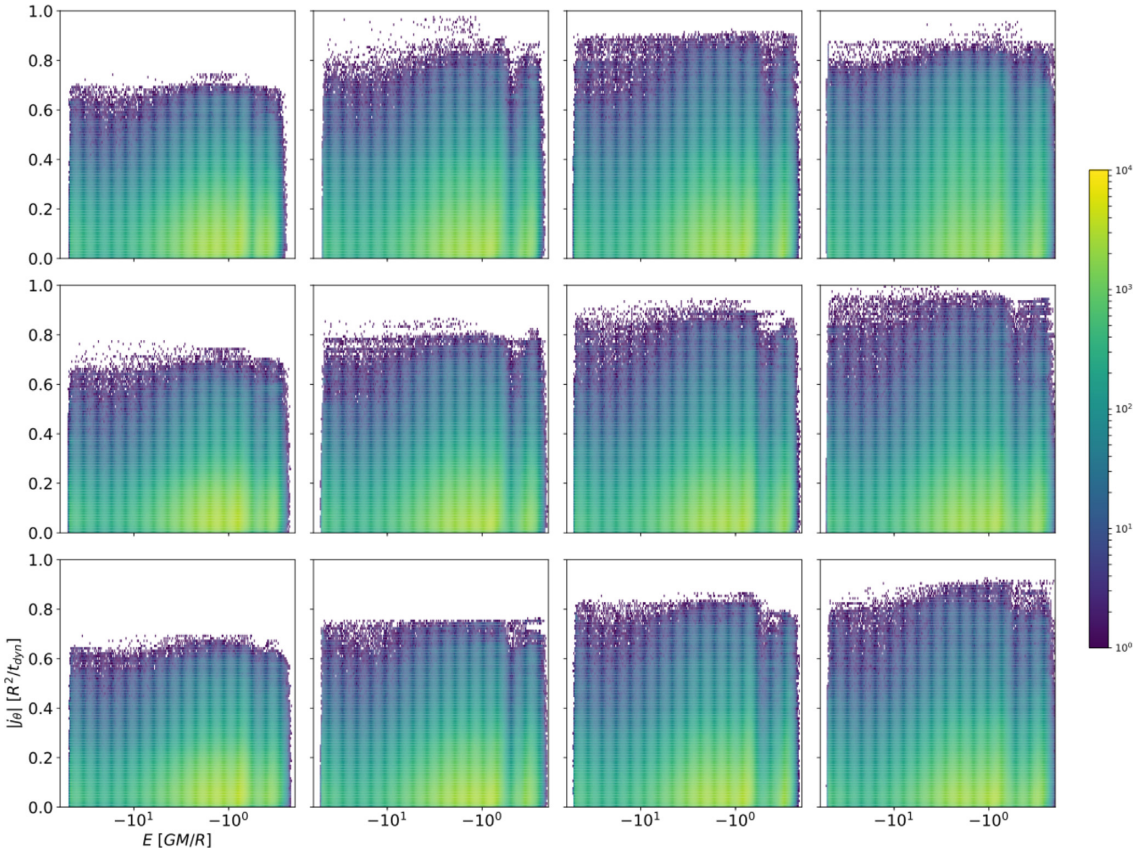

Figure C8. Classical binding energy and polar orbital action distributions of Gaussian isolated collapse simulations. Panels are organized by correlation (column wise: $C = 0.5, 0.75, 0.9, 1.0$ left to right) and spin (row wise: $\lambda = 0.0, 0.05, 0.1$ top to bottom). Samples are taken from 100 equally spaced frames during 10–$12t_{\rm dyn}$. Sample points are taken such that a particle is given a j_θ and an independent classical energy at each frame. Note that the projection along energy gives a higher resolution version of Fig. C6.

equilibrated DF (Binney & Tremaine 2008). The three desired integrals are approximated here with three accessible actions. Two of the actions are tangential

$$j_\phi = \boldsymbol{j} \cdot \hat{\boldsymbol{z}} \tag{C1}$$

$$j_\theta = |\boldsymbol{j} - j_\phi \hat{\boldsymbol{z}}| \tag{C2}$$

and are expected to be approximately integrals of the motion. The third independent action is taken to be the conjugate to radius from its Fourier transform into frequency space, j_r, providing harmonic weights over the two extended dynamical times of sampling. Note that the $\hat{\boldsymbol{z}}$ vector used in j_ϕ aligns with the direction of net spin for haloes with $\lambda > 0.0$. For spin-less haloes, $\hat{\boldsymbol{z}}$ is chosen as the direction of greatest angular momentum dispersion, consistent with the spun halo orientation in the presence of an ROI. Classical energy will also be used as an approximate substitute for the radial action.

Probability DFs in higher dimensions provide a more detailed understanding of the DFs, and are used to good effect here due to the higher count statistics. Action distributions show some obvious changes in global structure (Fig. C7). Both transverse and radial actions show more compact support, much like the one-dimensional angular momentum action of Section C1. Some finer-structure changes are also visible in the transverse actions, perhaps due to their relation to the ROI. The compactification of the radial action with correlation implies fewer high-frequency radial modes are excited. The consistent reduction in width support along all three actions in Gaussian Bose haloes is similar to the compactification of motion that has been seen in other degrees of freedom presented earlier. The action supports vary with solid-body spin for classical collapse, but dependence of support with respect to spin is somewhat reduced when the XC interaction become sizable.

The energy spectra of halo samples over transverse actions show bands of relative overpopulation and underpopulation, features present in a single snapshot, and becoming visibly enhanced in stacking (Fig. C8). Some of these features may be related to 'back-splash shells' from first shell crossings (Mansfield, Kravtsov & Diemer 2017) or other processes, especially deeper in the potential well. The narrower bands show a great deal of variablilty with correlation, such that it is difficult to see how one set of bands in one halo may continuously deform into another, though they remain relatively consistent across spins. A small but pronounced sub-set of energy bands are visible at each correlation, like the main features of the one-dimensional energy distribution of Fig. C6. Little deformation of the bands occur with different transverse action.

How the actions change throughout the halo, which are represented here by the particle's mean orbital radius, we also hold signatures of Bose physics. Tangential actions show a distinct transition between the virialized and unvirialized regions (Fig. C9). Classical haloes show quasi-uniform spectra within the virial radius, then transitioning discontinuously to a sparser population. The transition across the virial boundary becomes weaker for more highly correlated haloes, producing a smoother and more homogeneous distribution. Fine structure is not well resolved along this action due to the minimal force in the transverse directions.

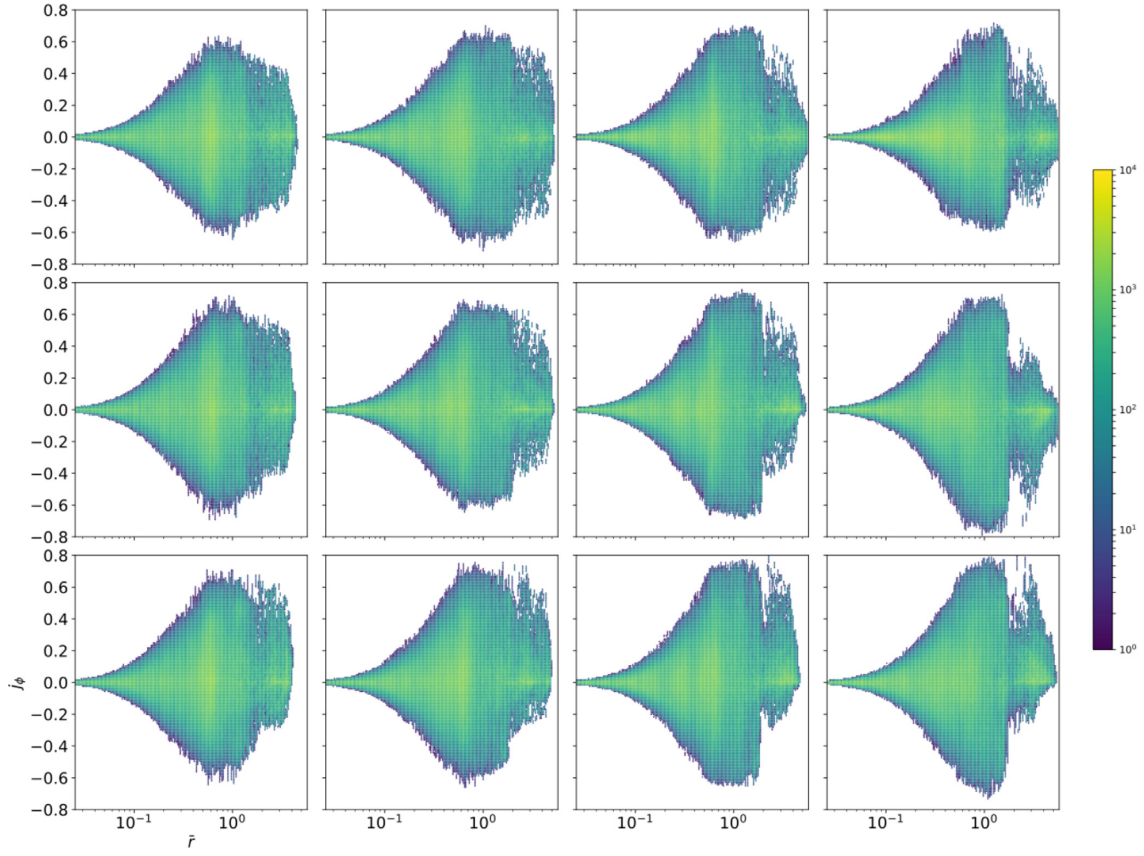

Figure C9. Azimuthal orbital action and mean orbit radius distributions of Gaussian isolated collapse simulations. Panels are organized by correlation (column wise: $C = 0.5, 0.75, 0.9, 1.0$ left to right) and spin (row wise: $\lambda = 0.0, 0.05, 0.1$ top to bottom). Samples are taken from 100 equally spaced frames during $10–12t_{\rm dyn}$. Sample points are taken such that each particle is given one mean radius and an independent j_ϕ at each frame.

C4 Further discussion

Fluid elements of Bose DM are subject to forces larger than that of Newtonian gravity at the halo centre and weaker than at the halo's edge. Variance in force in Gaussian haloes orders well with velocity dispersion variation of those same haloes. In the presence of near-identical spatial distributions, we consider the change of force variation throughout a halo as evidence of effective velocity dependence in the XC interaction. Further, there may be an opportunity to observe this force variation via the sub-structure of major haloes. If it is found that the matter in haloes and their sub-structure remain correlated to one another, it is possible that the forces experienced by the Bose DM sub-structure, such as satellite galaxies, are also altered relative to the classical case. The gravity felt by baryons within a satellite galaxy would be dominated by the Newtonian potential and, being bound to the sub-halo, would be pulled along the modified orbit. The possible implications for sub-structure orbits and their organization will be actively pursued in future cosmological simulations.

Changes to the classical energy profile can accumulate differences to the order of $O(400(1-C)^2)$ per cent in Gaussian collapse, and larger differences are observed in Top-hat haloes. Unfortunately, current baryonic tracers measuring a halo's energy density are not developed enough to differentiate ab initio between Bose and classical structures. A more direct measure of the local DM energy distribution is needed in order to distinguish between bulk correlated and uncorrelated motion. Remote detection efforts searching for axion decay may have promise of detecting such differences (Kelley & Quinn 2017; Bull et al. 2018).

Changes to structure, even at the present level of coarse-graining, present windows to detection of the axion. The observed kinematical signatures of Bose physics such as variations of circular orbit speeds, enhanced velocity dispersion, and migration of the fractional speed distribution are all potentially visible in direct and indirect axion detection efforts (Lentz et al. 2017; Bull et al. 2018; Foster et al. 2018; Knirck et al. 2018). Further, violation of the classical binding energy condition in halo bodies is one of the more unique structures of Bose physics. Though the sub-population is small, of the order of a tenth of a per cent for $C = 0.5$, it would be a distinctive signature of XC physics. The absence of such a sub-population is not necessarily evidence of vanishing XC physics, though, as the sub-population's size also depends strongly on the form of the initial distribution.

The compactness of orbital actions among Gaussian haloes leads in the direction of interpreting XC as a force that maintains coherence, though the robust observables that have yet to be identified. The mechanism leading to coherence also appears to extend to the smoothing of classical boundaries such as the virial radius. Mixing across the virial barrier is very weak in classical infall. The XC force of Bose infall is known from Fig. B6 to point mostly radially outward at the virial radius. This outward-pointing force is suspected to have the effect of displacing virialized orbits from their classical trajectories into the classically un-virialized space, smoothing the transition between classical virialized and non-virialized regions. The mixing across the virial radius can also be viewed in a more traditional condensed-matter framework. Standard Fermi systems near condensation have an analogous barrier, the Fermi surface. Modification of chemical potentials,

including through XC interactions, often smear the Fermi surface, seen in a theory of quasi-particles on the barrier (Nozières 1964). Bose systems at zero temperature are also capable of forming quasi-particles (Leggett 2006). The non-local XC force of self-gravitating axions is akin to a chemical potential, being largely set by Lagrange multipliers of particle-number conservation. It is suspected that the XC's degradation of the virial barrier may be understood as the mixing of quasi-particle excitations. The effect this mixing has on the intergalactic media and the medium between halo and substructure remains to be seen. It may be that distinguishing between different virial volumes becomes ambiguous, which may impact the shape, mass, and motions of cosmological haloes and their substructure.

These impacts of Bose physics on a halo's angular momentum and speed distributions have a profound effect on the particles' local energy distribution. Axion DM searches using the decay of halo axions into photons are sensitive to these changes. We construct samples of energy spectra at the approximate solar radius $r = 0.05R$, one fiftieth the haloes' virial radius, to estimate the signal shapes that may be seen by DM searches (Fig. 12). The set of these signals in the halo centre frame, as may be observed in a radio telescope survey of a nearby galaxy (Kelley & Quinn 2017; Bull et al. 2018), show Bose structures that significantly depart from CDM and standard near-isothermal shapes. Depletion of the lone thermal-like peak in Bose spectra is accompanied by a large secondary peak at $K.E. = 4GM/R$. Either of these features may be a signature of Bose physics. Also, like the angular momentum and speed distributions of Figs C5 and B7, the overall width of the Bose energy spectra is somewhat narrower than their CDM counterparts. The circularly orbiting signals match what a terrestrial direct axion DM search may see (Brun et al. 2017; Du et al. 2018; Jeong et al. 2018; Zhong et al. 2018). The differences in shape seen in the halo-frame signals are somewhat reduced by boosting to a co-rotating circular orbit, though the new high-energy structure remains visible. Fine structure within the new high-energy peak, or elsewhere in the spectra, cannot be resolved with current simulations. More resolved and complete simulations will be needed to provide realistic signal shapes including this fine structure.

APPENDIX D: STRUCTURE CONVERGENCE

This study makes several simplifying numerical approximations, such as finite time-steps, force softening, and sample number. We perform several tests on the simulation output to quantify and minimize the impacts of these approximation parameters in the main analysis. The highlights of those analyses are provided here. We also look into the behaviour of finer structures with change of particle number as a text of convergence.

We will show that the finite integration of forces and kinetics over time produce minor errors in the evolution of the degrees of freedom, and in the continuum integral actions of motion. These errors may accumulate over successive integrations, altering the resulting state, especially in regions of fast evolution. Leapfrog integration is chosen for its stability with respect to quantities of phase-space integrals. Total classical energy is an example of one such quantity (Fig. D1). This shows energy conservation is well converged in Gaussian infall for time-steps of $0.5 \times 10^{-2} t_{\rm dyn}$ or smaller. Bose Gaussian haloes do show an accumulated bias on the 1 per cent level relative to the $\delta t = 0.25 \times 10^{-2} t_{\rm dyn}$ classical halo. The bias may be a consequence of XC and softening length interactions. Top-hat haloes behave similarly, though they require an increased softening length to control noise errors at the near-singular first crossing, yet still produce slightly higher error around first crossing as compared to a Gaussian halo. Force evaluation and

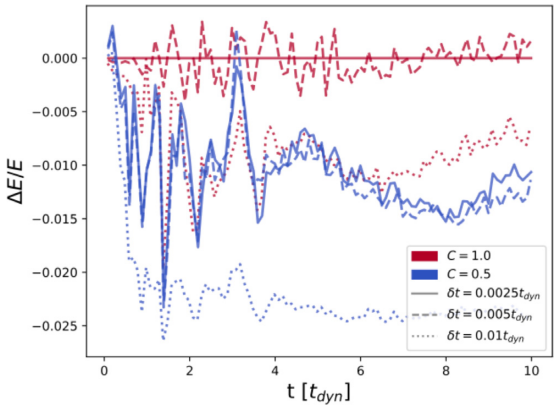

Figure D1. Relative total classical energy of halo over time for Gaussian isolated collapse simulations with different correlations and time-step size. Energy is relative to classical collapse with time-step resolution $0.25 \times 10^{-2} t_{\rm dyn}$. The period displayed is the $10 t_{\rm dyn}$ of initial simulation. Profile coloration indicates degree of correlation ranging from classical $C = 1.0$ to highly correlated $C = 0.5$. The haloes have no spin. Line style is given by step size in units of dynamical time.

kinetic evaluation are performed at double precision to minimize floating-point contributions to these errors.

Force softening limits the degree to which one can distinguish dynamical structure at some fraction of the softening length. The general rule for the simulations presented in the main text is to treat as spurious features much less than the softening scale. Softening kernel shape or extent can impact the halo's global structure via shot-noise fluctuations in the force from too large interparticle separations, or forcing biases from too complete overlap. There is an optimum length between these. One may find an optimal solution for the softening length with direct statistical techniques such as in Dehnen (2001), though we use the more heuristic approach of considering robust profiles such as density (Fig. D2). For 50 000 particle Gaussian haloes, smoothing much above or below $\epsilon = 1$, the sample-free softening length parameter of equation (19), produce an artificial depletion of mass at small radii, or other displacement of interior mass. Classical haloes appear to be somewhat more susceptible to mass migration than Bose. Top-hat collapses show an optimal softening length-scale at $\epsilon = 2$, much below which and the force noise disrupts the violent relaxation process. We find this sends the classical simulations nearer to a single power-law halo. In addition, Bose collapses appear especially susceptible to softening length change, and scattering of many of the particles at the singularity occurs if the softening is insufficient, resulting in a diffuse halo. Other aspects of XC sensitivity to softening are discussed below.

Total sample number provides the simplest subdivision of phase space as occupied by the presented haloes. Sample number impacts the simulations' degree of resolution in multiple observables. An adjusted softening length reduces the force errors some, but then introduces an enlarged intrinsic scale. The reduction in phase-space resolution leads to errors in observables. We show these errors with respect to particle number for several figures-of-interest of the main text. The softening length changes with particle number according to equation (19).

The radial density profile is approximately constant for nearly an order of magnitude in particle number, producing marginal depletion at inner radii (Fig. D3). Lowering particle number does eventually produce a shift of the outer power law and produces a complete depletion of the inner halo at $N = 1000$ for both classical and Bose haloes when using a softening length of $\epsilon = 1$. Increasing

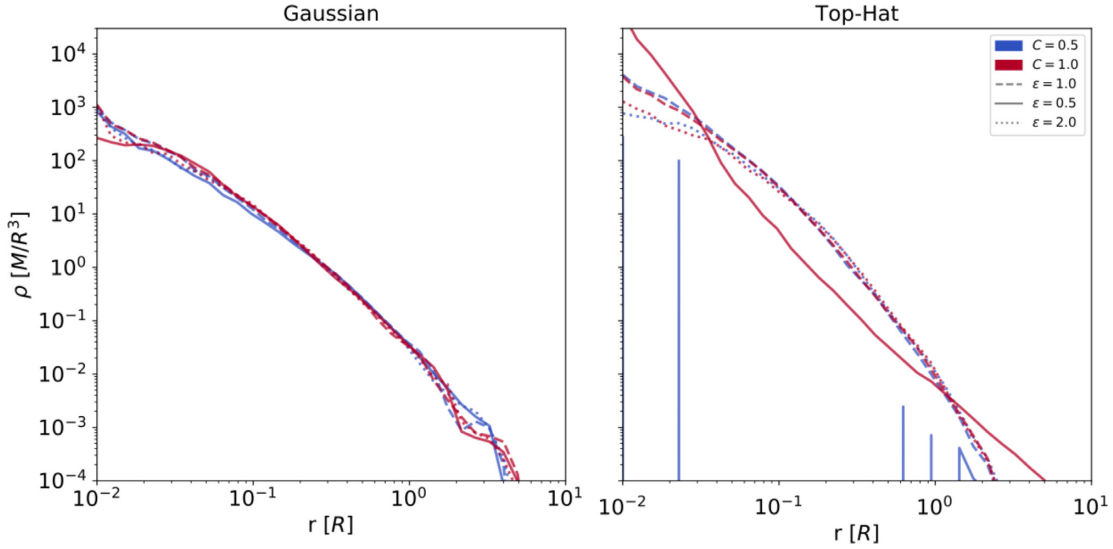

Figure D2. Radial density profiles of the isolated collapse simulations with different softening length. (Left) Gaussian profiles and (Right) Top-hat profiles. Haloes were measure after evolving for $10t_{\rm dyn}$. Profile coloration indicates degree of correlation ranging from classical $C = 1.0$ to highly correlated $C = 0.5$. Haloes have no spin. Line style indicates size of $K1$ softening length. ε refers to the softening size relative to the shape-dependent central value defined in the text.

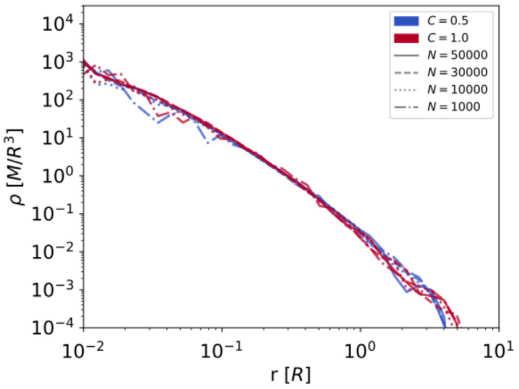

Figure D3. Radial density profiles of the Gaussian isolated collapse simulations with different particle number. Haloes were measured after evolving for $10t_{\rm dyn}$. Haloes are without spin. Profile coloration indicates degree of correlation ranging from classical $C = 1.0$ to highly correlated $C = 0.5$. Line style indicates number of particles. Simulations with greater than 10 000 samples use softening parameter $\epsilon = 1$, while 1000 particle simulations use $\epsilon = 2$ for the classical case and $\epsilon = 3$ for Bose.

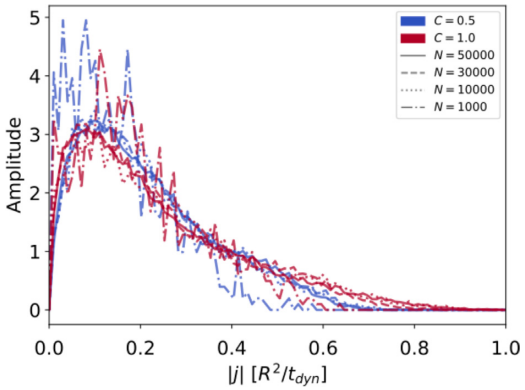

Figure D4. Magnitude angular momentum DF of the Gaussian isolated collapse simulations with different particle count. Haloes were measured after evolving for $10t_{\rm dyn}$. Haloes are without spin. Profile coloration indicates degree of correlation ranging from classical $C = 1.0$ to highly correlated $C = 0.5$. Line style indicates number of particles. Simulations with greater than 10 000 samples use softening parameter $\epsilon = 1$, while 1000 particle simulations use $\epsilon = 2$ for the classical case and $\epsilon = 3$ for Bose.

the softening length for the lowest sampled simulations to $\epsilon = 2$ puts the classical halo close to the universal profile, though the Bose halo requires $\epsilon = 3$ to prevent the severe depletion mentioned above.

Distribution of the magnitude angular momentum is also consistent in the mean for haloes of sampling above 10 000 (Fig. D4). Binning noise above the mean signal is of Poisson type for these higher resolution haloes, scaling with $1/\sqrt{N}$ samples per bin. Haloes below 10 000 particles are also seen to change the width. Both $N = 1000$ simulations shown become narrower as force softening, which are set to $\epsilon = 2$ for classical and $\epsilon = 3$ for Bose, reduces the strength of the symmetry-breaking ROI, which sets the spread in angular momentum.

Lastly, we observe the resonance structure observed in the radial orbital action (Fig. D5). Much of the structure discussed in the text at 50 000 samples remains visible at 30 000. Fine structure is more difficult to resolve for simulations with 10 000 samples. The smallest simulations have either no or too few particles with orbital radii much below the initial condition length-scale $r = R$ to see virial resonances. Some of the resonant orbits not yet virialized can be seen even at $N = 1000$.

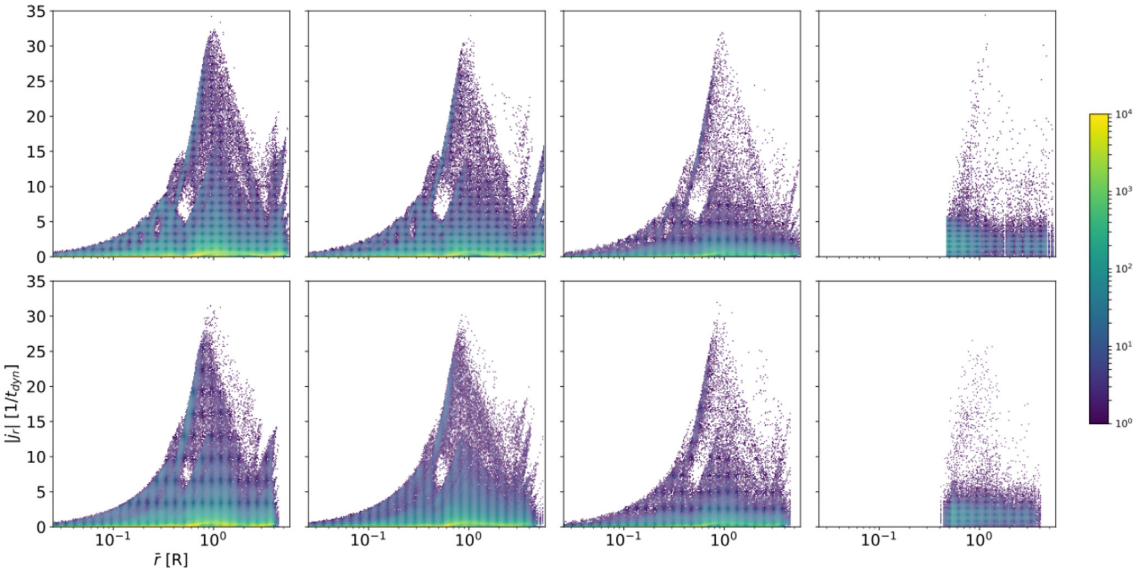

Figure D5. Radial orbital action and mean orbit radius of Gaussian isolated collapse simulations. panels are organized by correlation (column wise: 0.5, 0.75, 0.9, 1.0 left to right) and spin (row wise: 0.0, 0.05, 0.1 top to bottom). Samples are taken from 100 equally spaced frames during 10–12$t_{\rm dyn}$. Sample points are taken such that each particle is given a single mean radius and the radial autocorrelation power spectrum. Haloes are without spin. Simulations above 10 000 samples use softening parameter $\epsilon = 1$, while 1000 particle simulations use $\epsilon = 2$ for the classical case and $\epsilon = 3$ for Bose.

This paper has been typeset from a TEX/LATEX file prepared by the author.